Journal of Environmental Chemical Engineering 6 (2018) 1333–1346

Contents lists available at ScienceDirect

Journal of Environmental Chemical Engineering

journal homepage: www.elsevier.com/locate/jece

Isotherm and kinetic investigations on the adsorption of organophosphorus pesticides on graphene oxide based silica coated magnetic nanoparticles functionalized with 2-phenylethylamine

V.W.O. Wanjeri[a], C.J. Sheppard[b], A.R.E. Prinsloo[b], J.C. Ngila[a], P.G. Ndungu[a,*]

[a] University of Johannesburg, Department of Applied Chemistry, Centre for Nanomaterials Science Research, Energy, Sensors and Multifunctional Nanomaterials Research Group, P.O. Box 17011 Doornfontein 2028, South Africa

[b] Chromium Research Group, Department of Physics, University of Johannesburg, Auckland Park, South Africa

ARTICLE INFO

Keywords:
Organophosphorus pesticides
Graphene oxide
Core shell nanoparticles
Magnetic solid phase extraction
Adsorption capacity

ABSTRACT

The study describes the preparation of graphene oxide based silica coated magnetic nanoparticles (Fe_3O_4@SiO_2@GO) functionalized with 2-phenylethylamine (PEA) as an adsorbent for selected organophosphorus pesticides (OPPs) namely chlorpyrifos, parathion, and malathion from aqueous solution. The synthesised (Fe_3O_4@SiO_2@GO-PEA) adsorbent was characterised using Fourier transform-infrared (FT-IR) spectroscopy, transmission electron microscopy (TEM), X-ray diffraction (XRD), Zeta potential, Nitrogen adsorption/desorption at 77 K, and a Vibrating Sample Magnetometer (VSM). The maximum adsorption was found at 15 min, with 15 mg adsorbent dosage using 1 μg/mL concentration. There was no significant difference in the pH condition used highlighting the potential to use the material on a variety of samples. Using non-linear methods, the sorption isotherm data were fitted to Langmuir, Freundlich, Temkin, Dubinin–Radushkevich, Sips, and Redlich and Peterson models. All three pesticides were best fit with the Sips model. Pseudo-first and pseudo-second order kinetics models were fitted to the experimental data using non-linear methods, and pseudo-second-order kinetics gave the best fit to the data for all three pesticides. The absorbent was tested for its reusability, and there was little loss in the recovery of OPPs after 10 cycles. Finally, the adsorbent was tested using real world samples from the Vaal River and Dam (South Africa), and showed greater than 86.9% recovery. The results obtained showed that the synthesised Fe_3O_4@SiO_2@GO-PEA is an efficient adsorbent for recovery and analysis of pesticides.

1. Introduction

Organophosphorus pesticides (OPP) are among the most extensively used pesticides in the world today, and this is mainly due to the widespread ban, since the 1970s, on organochloride pesticides [1,2]. OPPs are relatively low cost, have a broad spectrum of activity, and have a high efficiency on a wide variety of pests [3]. However, despite their numerous advantages, the extensive and/or inappropriate use of OPPs has become a major risk to human health and the environment due to contamination of water, soil and agriculture produce [2,4].

Recent studies have confirmed that some OPPs are carcinogenic and mutagenic. In addition, some have a structure similar to organophosphorus nerve gases such soman and sarin, and thus are highly neurotoxic. The neurotoxicity can be ascribed to the irreversible inhibition of the enzyme acetylcholinesterase, an enzyme that regulates acetylcholine, a neurotransmitter needed for proper nervous system function [5–8]. Thus, repeated exposure to even low levels of OPPs for a long period of time can lead to accumulation of OPPs in the body and can result in long-term neurotoxic effects, related to the inhibition of neuropathy target esterase. This causes dysfunction of many autonomic and behavioural systems, eventually leading to respiratory, weakness or paralysis of the muscles and eventually death [1,9,10]. The United States Environmental Protection Agency (US-EPA) lists OPPs as either highly or moderately toxic. This is because, under optimum environmental conditions, they tend to degrade to products which are more toxic than the primary pesticide [11]. Due to the toxicity of OPPs, European Union Directive on drinking water quality (98/83/EC) has established a maximum allowed concentration of 0.1 ng/mL for each individual pesticide and 0.5 ng/mL for total pesticides [4,12].

Different adsorbent materials such as activated carbon, polymers, multi-walled carbon nanotubes and graphene have been used in the removal of pesticides from water. Among these adsorbents, graphene oxide (GO) has been reported as an excellent adsorbent and extraction material due to its exceptional physical and chemical properties which

* Corresponding author.
E-mail address: pndungu@uj.ac.za (P.G. Ndungu).

https://doi.org/10.1016/j.jece.2018.01.064
Received 13 September 2017; Received in revised form 23 January 2018; Accepted 26 January 2018
Available online 31 January 2018

include high adsorption capacity, strong mechanical, thermal properties and large specific surface area (theoretical value of 2630 m^2/g) [13,14]. In addition, GO has been applied in various analytical techniques due to its high density of oxygen functional groups (carboxyl, hydroxyl, carbonyl, and epoxy) on the carbon lattice [13,15]. These oxygen functionalities makes GO a hydrophilic material and provide the affinity toward a large number of compounds through different interactions like electrostatic interaction, hydrogen bonding, and π–π stacking dispersion forces [11]. However, when GO is dispersed into aqueous based sample solutions, removal either through high-speed centrifugation or strong filtration tends to be tedious and time-consuming [16,17].

Magnetic nanomaterials, especially magnetite (Fe_3O_4) nanoparticles (NPs), have attracted tremendous interest in research work concerned with the removal of pollutants from aqueous solutions [18]. This is because, Fe_3O_4 NPs have a high surface area, excellent ferromagnetic properties, are relatively less toxic than other NPs, and are easy to synthesize and functionalize [19]. However unprotected Fe_3O_4 nanoparticles tend to have a high chemical activity which is enhanced by the large surface area to volume ratio and strong dipole–dipole attractive forces on the surface of the particles [20]. In addition, Fe_3O_4 nanoparticles are highly susceptible to oxidisation in air which can result in significant loss of the various beneficial properties [21]. To prevent such limitations, magnetic nanoparticles can be protected by a layer of different materials such as silica, polymer, or noble metals, which can aid in maintaining individual particle stability and durability [22]. Coating Fe_3O_4 nanoparticles with silica (SiO_2) has several advantages which include protecting the Fe_3O_4 from oxidation, preventing aggregation, improving chemical stability, reducing the toxicity of the NPs, and the SiO_2 can serve as a platform to integrate other moieties or nanostructures through covalent bonds [11,21].

Thus, in this study, graphene oxide based silica coated with magnetic nanoparticles (Fe_3O_4@SiO_2@GO) functionalized with 2-phenylethylamine (PEA) was synthesized and characterized using various analytical techniques. The PEA was used to provide the hydrophobic and π-stacking interaction that enhances the adsorption of the OPPs on the adsorbent [2]. The prepared Fe_3O_4@SiO_2@GO-PEA was used in the removal of chlorpyrifos malathion and parathion (Fig. 1) from aqueous solution. The effect of solution pH, adsorbent dosage, contact time temperature and concentration in the adsorption of chlorpyrifos malathion and parathion were investigated.

The investigation of OPPs adsorption processes on nanocomposite materials and the generation of isotherm models, and kinetic data is important for several reasons. These include, predicting the behavior of OPPs on complex surfaces for extraction or absorption processes, understanding the capacities of the nanocomposites, generating quantitative data that can be used for comparative studies, and designing suitable processes that maybe adapted in wastewater treatment or analytical techniques. There is limited information in the literature on isotherm, and kinetic data for OPPs on such heterogeneous surfaces like the Fe_3O_4@SiO_2@GO-PEA nanocomposite. Thus, the adsorption isotherm and adsorption kinetics were investigated in detail. Finally, the reusability and applicability of the nanocomposite on real world samples was tested.

2. Materials and methods

2.1. Chemicals and reagents

All chemicals used in this work were of analytical grade. Potassium permanganate (≥99.0%), hydrogen peroxide (30 wt.%), Iron (II) chloride ($FeCl_2{\cdot}4H_2O$, 98%), hydrazine hydrate (50–60%), Tetraethylorthosilicate (TEOS, 99%), (3-Aminopropyl) triethoxysilane (APTES, > 98%), 2-phenylethyl amine (PEA, 99%), N-(3-dimethylaminopropyl)-N- ethyl carbodiimide hydrochloride (EDC, 98%), and N-hydroxysuccinimide (NHS, 98%), were obtained from Sigma–Aldrich Ltd (South Africa). Sulfuric acid, phosphoric acid, Iron (III) chloride ($FeCl_3{\cdot}6H_2O$, 99%), hexane (HPLC grade), methanol (HPLC grade), acetone (HPLC grade), ethanol (99%), were purchased from Merck Chemicals (South Africa).

Pesticide analytical standards (chlorpyrifos, parathion, and malathion) were purchased from Sigma–Aldrich Ltd (South Africa). All pesticide standards were of 98–99% purity. Stock solutions of each compound with a concentration of 200 mg/L were prepared in HPLC-grade acetone. Working standards solutions were prepared by diluting the stock solutions to appropriate concentrations in acetone. The stock and working standards were all stored at 0 °C.

2.2. Synthesis of graphene oxide

Graphene oxide (GO) was synthesised from graphite powder by adapting the improved hummer method (Tour method) [23]. A 9:1 mixture of concentrated H_2SO_4/H_3PO_4 (360:40 mL) was added to a mixture of 3.0 g graphite powder and 18.0 g $KMnO_4$ in a 1 Litre round bottom flask. The flask was then placed in a 50 °C preheated oil bath and stirred for 12 h in a fumehood. The reaction mixture was then left to cool to room temperature and then poured into 400 mL of ice. Thereafter, 3 mL of 30% H_2O_2 was added dropwise. The mixture was centrifuged at 4000 rpm for 30 min, and the supernatant was decanted. The remaining solid material was washed in succession with 1 Litre of water, 200 mL of 30% HCl, and 200 mL of ethanol (2 times); for each wash, the mixture was placed in an ultrasonic bath for 5 min and then centrifuged at 4000 rpm for 30 min and the supernatant decanted. The material remaining after this extended multiple-wash process was coagulated with 200 mL of ether, and the resulting suspension was filtered through a PTFE (polytetrafluoroethylene) membrane with a 0.45 µm pore size. The solid obtained on the filter was vacuum-dried overnight at 40 °C.

2.3. Synthesis of iron oxide nanocomposite

Separate steps were used to synthesize the nanocomposite. These consisted of synthesizing the iron oxide nanoparticles, coating the iron oxide nanoparticles with silica, attaching a suitable linker to the silica surface, and finally covalently attaching the graphene oxide to the surface of the nanoparticles.

2.3.1. Synthesis of the iron oxide nanoparticles

The iron oxide (Fe_3O_4) was prepared using a modified co-precipitation method by using $FeCl_2{\cdot}4H_2O$ and $FeCl_3{\cdot}6H_2O$ as precursors

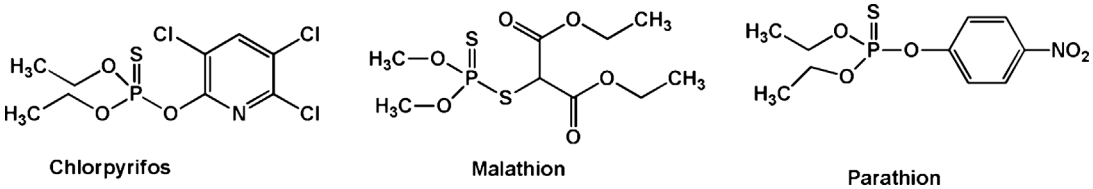

Fig. 1. Chemical structures of selected OPPs used in the study.

[24]. Briefly, the synthesis procedure involved preparation of a mixture of 5 mL of ammonia and 2 mL of hydrazine in 50 mL of deionized water in a 100 mL two neck round bottom flask. Then 20 mL of freshly prepared mixture of 1 g of $FeCl_2{\cdot}4H_2O$ and 2.7 g of $FeCl_3{\cdot}6H_2O$, in an aqueous solution, was added dropwise to the solution and stirred at 90 °C for 60 min in a preheated oil bath. The products were collected using an external magnet after cooling to room temperature and were washed alternately with water and acetone three times. Fe_3O_4 nanoparticles were then dried at 70 °C for 12 h in a vacuum oven.

2.3.2. Coating of silica on the iron oxide nanoparticles

$Fe_3O_4@SiO_2$-NH_2 was synthesised using Stober's method [14] where 0.5 g of prepared Fe_3O_4 nanoparticles were added to a solution containing a mixture 100 mL of ethanol and water in a ratio of 1:1 in a glass bottle with a PTFE (polytetrafluoroethylene) cap. Then 5 mL of 25% NH_4OH solution added and sonicated for 30 min to disperse the NPs. 2 mL of TEOS were then added and the contents allowed to stir at room temperature for 20 h. Thereafter, 2 mL APTES was added to the mixture and stirred for 6 h. The produced $Fe_3O_4@SiO_2$-NH_2 were magnetically separated using an external magnet, washed with water and ethanol several times and then dried in the oven at 70 °C for 24 h. A schematic illustrating the steps used to synthesize the $Fe_3O_4@SiO_2$-NH_2 nanoparticles is shown in Fig. 2.

2.3.3. Covalent coupling of graphene oxide to $Fe_3O_4@SiO_2$-NH_2 nanoparticles

The covalent coupling of graphene oxide to $Fe_3O_4@SiO_2$-NH_2 was carried out by inducing the amide bond formation [14], where 0.2 g graphene oxide was added to 400 mL deionized water and ultrasonicated for 2 h in a glass bottle with PTFE cap. Activation of −COOH groups on the graphene oxide was carried out by the addition of 0.2 g of N-(3-dimethylaminopropyl)-N-ethyl carbodiimide hydrochloride (EDC) and 0.160 g N-hydroxysuccinimide (NHS) into the graphene oxide/water suspension. The mixture was vigorously stirred using a magnetic stirrer at 400 rpm for 2 h. Then 0.4 g of $Fe_3O_4@SiO_2$-NH_2 dispersed in water was added slowly to the mixture and ultra-sonicated for another 30 min. Finally, the reaction was carried out at 80 °C for 1 h under strong stirring in a preheated oil bath. The $Fe_3O_4@SiO_2$-GO particles were separated by an external magnetic field and washed with water several times and dried in an oven for 12 h at 70 °C.

In modification of the graphene oxide nanocomposite with PEA, a combination of 1.0 g $Fe_3O_4@SiO_2$-GO particles, 30 mg of EDC and 20 mg of NHS were added in 100 mL water then ultrasonicated for 30 min. 5 mL methanol containing 0.5 g 2-phenylethyl amine was added to the mixture and stirred for 30 min. Finally, the mixture was refluxed for 1 h at 80 °C in a pre-heated oil bath to obtain $Fe_3O_4@SiO_2$@GO-PEA. The obtained nanocomposites were washed with ethanol and water several times and then dried in the oven at 60 °C for 12 h [2].

2.4. Characterization

The structural composition, morphological features and physiochemical properties of graphite, graphene oxide, Fe_3O_4 NPs, and the various nanocomposites ($Fe_3O_4@SiO_2$—NH_2, $Fe_3O_4@SiO_2$-GO and $Fe_3O_4@SiO_2$@GO-PEA) were studied using different characterization techniques. Fourier transform infrared (FTIR) spectra of the samples were obtained using Perkin Elmer Spectrum 100 from 400 to 4000 cm^{-1}. The samples were prepared by grinding 1 mg of the sample with 100 mg of KBr, and the mixture compressed with a hydraulic press to form 1 mm thick pellet discs. The spectra were obtained at room temperature with KBr disk serving as the background. Transmission Electron Microscopy (TEM) was done using a JEOL JEM-2100F Field Emission Electron microscope instrument equipped with a Lab6 source at an accelerating voltage of 200 kV. The images were captured using Gatan Orius CCD camera controller. Samples used for TEM analysis were prepared by dispersing the nanoparticle powder in ethanol followed by ultrasonication for 10 min. A drop of the dispersion was placed onto coated copper grid (200 mesh size Cu-grid). X-ray diffraction (XRD) was determined with a PANalytical X'Pert PRO X-ray diffractometer using Cu Kα radiation with a wavelength of 1.5406 Å at 40 kV and 40 mA in a range of 4–90° of 2θ at room temperature. Nitrogen adsorption/desorption isotherm analysis was used to determine the BET surface area, pore volume and the average pore diameter were assessed according to the Barret–Joyner–Halenda (BJH) using a Micrometrics ASAP 2020 (Atlanta, Georgia, USA). The surface charge and point of zero charge of the nanocomposites were determined using Zeta sizer ZEN 3600, Malvern. The samples were prepared by dispersing 3 mg nanocomposites in 10 mL water at varying pH (2, 4, 6, 8, 10, 12,). The pH was adjusted with 0.1 M of HCl and 0.1 M NaOH solution using Ohous ST20 pH meter. Point of zero charge was obtained by plotting the zeta potential verses the pH and the surface charge was reported as an average value.

2.5. Analytical methods

The extracted OPPs were analysed using 7890 Agilent GC coupled to a PEGASUS 4D Time of Flight mass spectrometer (GC-TOF/MS) with an Agilent autosampler (Agilent Technologies, Santa Clara, CA). Separation was carried out using an RXi-5Sil- MS capillary column (30 m × 0.25 mm, 0.25 µm, contained 5% phenylmethyl polysiloxane). For the chromatographic determination, helium (99.999%) was used as the carrier gas at a constant flow rate of 1 mL/min. The injector temperature was kept at 250 °C in splitless mode (5 min), and the oven temperature was programmed as follows: initial temperature 100 °C (hold 2 min), 20 °C/min to 180 °C, and 10 °C/min to 250 °C (hold 2 min) The MS ionization was carried out in the electron ionization mode. The spectra were obtained at 70 eV. The GC–MS interface and the ion source temperature were set at 250 °C and 200 °C, respectively. The spectra obtained was processed using Restex pesticide and Korea pesticide library. The minimum similarity match was set at 750.

2.6. Adsorption isotherms and kinetic studies

The adsorption experiments using aqueous solutions of parathion, malathion and chlorpyrifos were performed using thermostatic water bath shaker with a shaking speed of 120 rpm. Experiments were done in

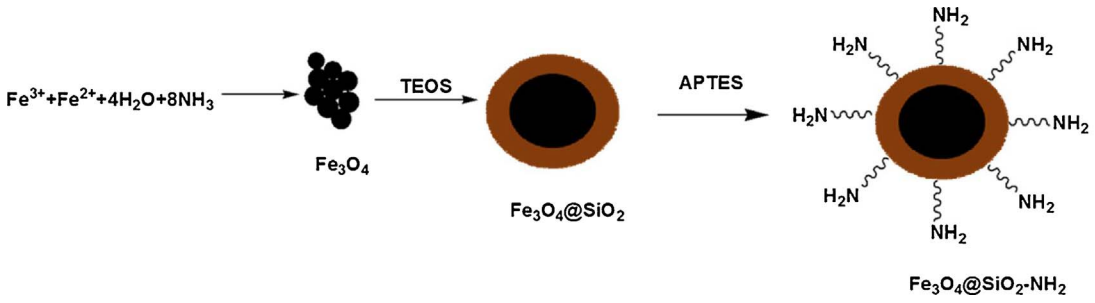

Fig. 2. Synthesis of $Fe_3O_4@SiO_2$ and $Fe_3O_4@SiO_2$-NH_2.

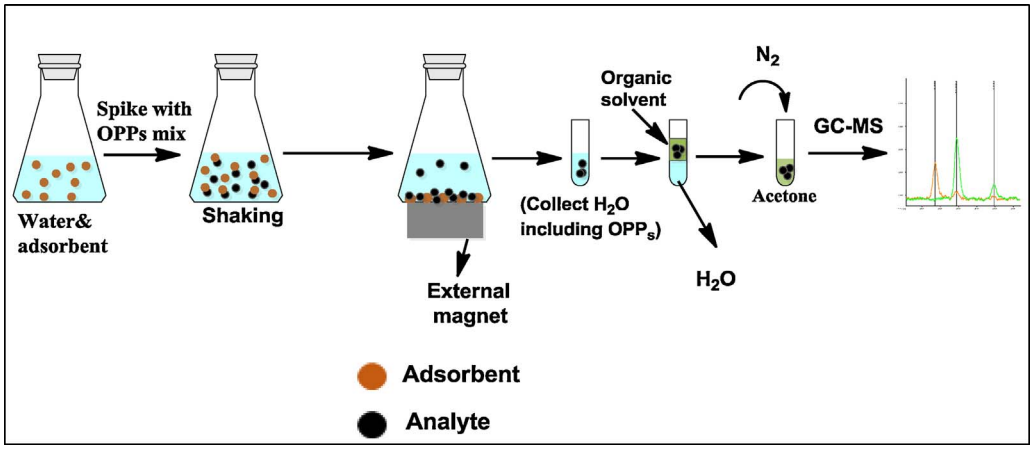

Fig. 3. Schematic representation of the magnetic solid phase extraction procedure for adsorption studies on selected OPPs.

triplicates. Different adsorption parameters such as the solution contact time, pH and amount of adsorbent dose were optimised at 25 °C in 100 mL conical flask containing 10 mL of water spiked with 1 µg/mL of parathion, malathion and chlorpyrifos mix. Adsorbent dosage effect in the adsorption of parathion, malathion and chlorpyrifos pesticides were studied in the range of 2–40 mg while the effect of solution pH was studied at a pH range of 3.0–11.0. The pH of different solutions was adjusted with 0.1 M NaOH and 0.1 M HCl solutions. After magnetic separation, 10 mL of aqueous solution was extracted three times with 2 mL n-hexane (vortex assisted for 1 min). This was concentrated to dryness under nitrogen gas and the solvent exchanged to acetone which was further dried to 500 µL (Fig. 3). Finally, 1.0 µL of the extract was injected to GC-TOF/MS. The percentage recovery of parathion, malathion and chlorpyrifos was calculated using Eq. (1).

$$\% \text{ Removal} = \frac{C_o - C_e}{C_o} \times 100 \quad (1)$$

where C_o (mol L^{-1}) is the initial concentration of solution before adsorption and C_e (mol L^{-1}) is the final concentration after the adsorption of the selected pesticides.

After the optimisation of the pH, contact time and adsorbent dosage, the adsorption capacity was studied with a concentration ranging from 0.3–5 µg/mL using the optimum conditions obtained. The equilibrium adsorption was calculated using Eq. (2) [25,26].

$$q_e = \frac{V}{m}(C_o - C_e) \quad (2)$$

where q_e is the adsorption capacity, V is the initial volume of the sample before pretreatment, m is the mass of the applied adsorbent for adsorption, C_O is the initial concentration and C_e is the residual concentration of an analyte in the solution produced after adsorption.

Kinetics study were conducted with a time range of 1–60 min. All experiments were done in triplicates. At regular intervals, the sample was removed, thereafter the adsorbent removed using an NdFeB external magnet and the unadsorbed OPPs extracted using hexane as described in Section 2.6 and Fig. 3. The amount of OPPs at different time intervals were calculated using Eq. (3) [27].

$$q_t = \frac{V}{m}(C_o - C_t) \quad (3)$$

where, q_t, is the amount of the analyte adsorbed per unit mass at time t, C_o denotes the initial concentration of the solution and C_t is the concentration at time t that remained in the solution.

3. Results and discussion

3.1. Characterization of the adsorbent

The synthesized Fe_3O_4@SiO_2-GO-PEA was intensively characterized using different analytical techniques such as FT-IR, TEM, XRD, Zeta potential, Nitrogen adsorption/desorption and magnetization using the vibrating sample magnetometer (VSM) to confirm the physical, chemical and morphological properties of the synthesized Fe_3O_4@SiO_2-GO nanoparticles further functionalized with 2-phenylethylamine.

3.1.1. FTIR spectral analysis

The FTIR spectra of graphene oxide, Fe_3O_4, Fe_3O_4@SiO_2-NH_2, and Fe_3O_4@SiO_2-GO-PEA are presented in Fig. 4. The spectrum for graphene oxide (Fig. 4a) showed a broad peak at 3418 cm^{-1}, which is due to O—H stretching vibrations. The peaks at 1738 cm^{-1} and 1624 cm^{-1} are due to the carboxyl stretching of C═O and aromatic functional group C═C respectively. Absorption peak at 1418 cm^{-1} can be ascribed to C—C stretching/vibrations. The peaks at 1228 cm^{-1} and 1055 cm^{-1} are due to C—O epoxy stretching and alkoxy stretching respectively. These functional groups on the graphene oxide nano-sheets confirms the introduction of oxygen groups onto the graphene

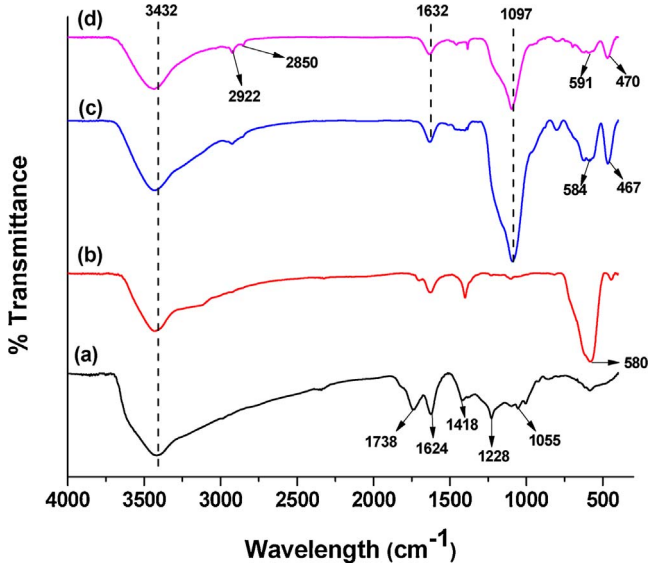

Fig. 4. FTIR spectra of GO (a), Fe_3O_4 (b) Fe_3O_4@SiO_2-NH_2 (c) and Fe_3O_4@SiO_2-GO-PEA (d).

backbone and is indicative of separation of the graphene sheets from the parent graphite materials during the oxidation process [11,28–30]. The Fe_3O_4 spectrum (Fig. 4b) showed characteristic vibrational stretching band at about 580 cm^{-1} due to Fe—O bonds. No higher frequency band at 632 cm^{-1} was observed, which is the characteristic peak of ɣ- Fe_2O_3. This is a good indication that pure magnetite Fe_3O_4 was formed. The peak at 3432 cm^{-1} and 1630 cm^{-1} are assigned to the —OH stretching vibration due to the existence of surface hydroxyl and H_2O on the Fe_3O_4 nanoparticles [31].

After coating Fe_3O_4 with silica and modifying with an amine group (Fig. 4***c***), Fe_3O_4@SiO_2-NH_2 showed peaks at 1097 cm^{-1}, 803 cm^{-1} and 467 cm^{-1} which were a result of asymmetric stretching vibrations of the Si—O—Si bond, the symmetric stretching of Si—O—Si, and the bending vibration of the Si—OH bond, respectively [32,33]. The peaks at 2836 cm^{-1} and 2928 cm^{-1} were due to the C—H stretching vibration of the hydrocarbon chains from amino propyltriethoxysilane [34]. It was also observed that the characteristic peak corresponding to the stretching vibration of Fe—O bond shifted indicating that the Fe_3O_4 was influenced by silica coating due to the formation of Fe-O-Si bond [33,35]. The absorption peak at 3432 cm^{-1} in Fig. 4 curves (b) and (c) is due to adsorbed water on the silica shell [32,36].

For the reaction between Fe_3O_4@SiO_2-NH_2 and the graphene oxide nanosheets, the amino functional group was covalently bonded to the nanosheets through the formation of an amide bond [14]. The product Fe_3O_4 @SiO_2-GO was further modified using 2-phenylethyl amine to provide more active sites (Fig. 4***d***). The disappearance of the peak at 1738 cm^{-1} (—C═O group) was observed and new characteristic peaks of amide carbonyl group were observed at 1632 cm^{-1} and 1425 cm^{-1} which correspond to —CONH amide band and C—N stretch of amide respectively [2,14,37]. This result confirms that the graphene oxide was successfully attached to Fe_3O_4@SiO_2-NH_2 magnetic nanoparticle. Finally, each nanomaterial has a broad peak in the 3400 cm^{-1} region, which are due to O—H stretching vibrations from surface sorbed water, which indicates the adsorbents have favorable surfaces for hydrogen bonding interactions.

3.1.2. Transmission electron microscopy (TEM) observations

The morphology of Fe_3O_4@SiO_2-GO-PEA nanocomposite was analysed using TEM, and the images are presented in Fig. 5. The prepared Fe_3O_4 nanoparticles were found to be spherical in shape and agglomerated (Fig. 5a) due to the high surface charge on the Fe_3O_4 nanoparticles and magneto dipole interactions [31]. The nanoparticle diameter before and after silica coating was measured using Image J (Java-based). The Fe_3O_4 nanoparticles had an average particle diameter of 12.3 ± 3 nm and on coating with silica, the silica thickness was found to be 9.9 ± 2 nm. This confirmed the formation of a silica layer around the Fe_3O_4 nanoparticle. The graphene oxide material seen in Fig. 5c showed characteristic irregular and wrinkled nanosheets, usually ascribed to the tendency of the separate sheets to self-assemble and form multilayer aggregation [38]. This is mainly due to the electronegativity of oxygen atom of —OH and —COOH groups on the graphene oxide layer which results in aggregation of the individual sheets [39]. Graphene oxide was also observed to be transparent under the electron beam, which confirmed the existence of two-dimensional nanosheets of graphene oxide [40]. Fe_3O_4@SiO_2@GO-PEA nanocomposite (Fig. 5d) shows the successful attachment of Fe_3O_4@SiO_2-NH_2 nanoparticle to the graphene oxide nanosheet like structure. This confirms the FTIR results which demonstrated that the Fe_3O_4@SiO_2-NH_2 nanoparticle were covalently bonded to graphene oxide through an amide bond [34,41].

3.1.3. X-ray diffraction (XRD) results

The crystalline structure of Fe_3O_4, nanoparticles before and after silica coating were analyzed using powder XRD technique and the results are illustrated in Fig. 6. Graphene oxide presented a broad and weak diffraction peak at 2θ = 10° with a d-spacing of 0.95 nm, corresponding to the (002) plane [23,42]. The increase in d-spacing from 0.34 nm may be due to the introduction of oxygen functional groups on the surfaces of the graphite parent material and subsequent separation of the graphene sheets into graphene oxide nanosheets [11,43]. Fe_3O_4 showed diffraction peaks with 2θ at 30°, 35.5°, 43°, 53.5°, 57° and 62° which corresponds to the crystal planes of (220), (311), (400), (422), (511), and (440) respectively. This is indicative of cubic spinel structure of the magnetite [44] which conforms with the reported values of ICDD pdf # 04-006-6497. The diffraction peak 35° (311) with a d-spacing of 0.252 nm at 2θ was used to calculate the crystallite size of the Fe_3O_4 nanoparticle using the Debye-Scherrer formula (Eq. (4));

$$D = \frac{K\lambda}{\beta \cos\theta} \quad (4)$$

where D is the average crystallite size, λ is the X-ray wavelength (0.154 nm), β is the corrected width of the XRD peak at full width at

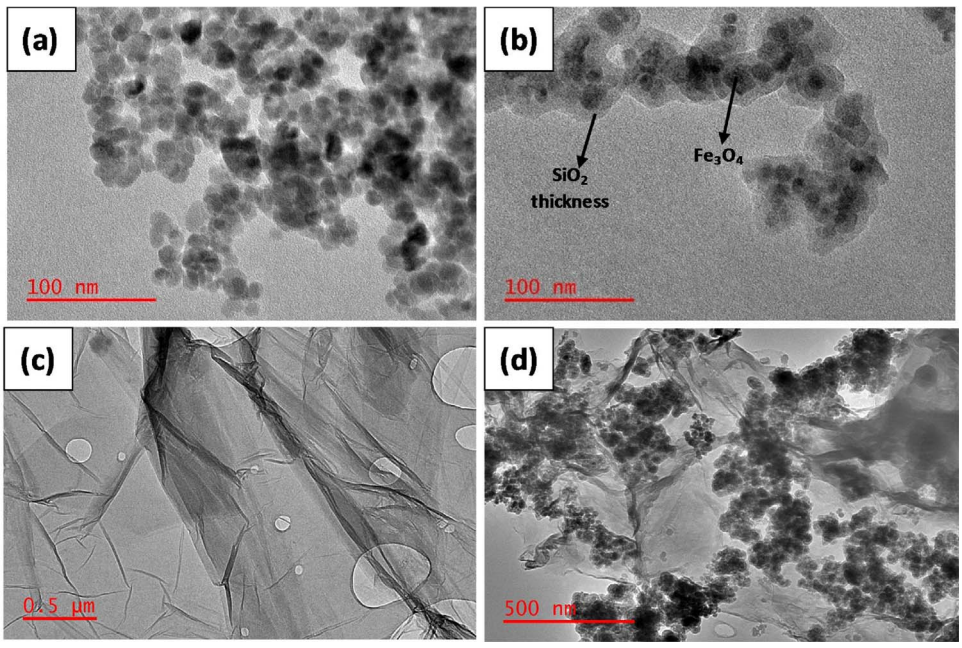

Fig. 5. TEM images of Fe_3O_4 (a), Fe_3O_4@SiO_2-NH_2 (b), GO (c) and Fe_3O_4@SiO_2-GO-PEA (d).

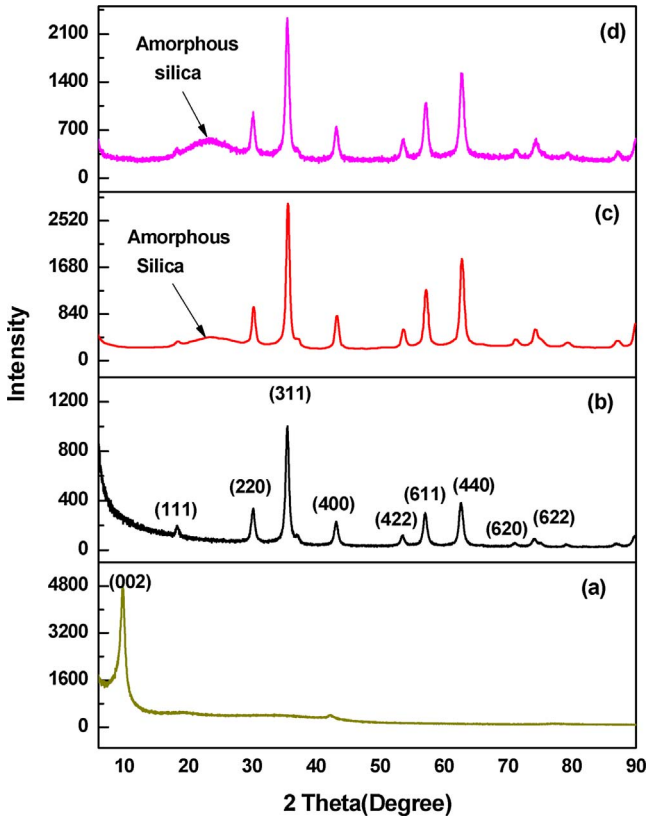

Fig. 6. XRD diffraction patterns of graphene oxide (a), Fe_3O_4 (b), Fe_3O_4@SiO_2-NH_2 (c) and Fe_3O_4@SiO_2-GO-PEA (d).

half maximum (FWHM) and K is a shape factor which is approximated as 0.9 for magnetite [45,46]. The calculated crystallite size of Fe_3O_4 was estimated to be 10.4 nm.

After silica coating process and modification with the amine group, Fe_3O_4@SiO_2-NH_2 nanoparticles were analysed and indexed using the International Centre for Diffraction Data powder diffraction file (ICDD pdf) # 04-013-9807 (Fig. 6). Fe_3O_4@SiO_2-NH_2 nanoparticles showed a similar diffraction pattern to that of the Fe_3O_4 core with no significant change in the d-spacing at 2θ except for a broad peak observed between 21°−27°, and decrease in the intensity of Fe_3O_4 nanoparticles. This is mainly due to the formation amorphous structure of silica layer on the Fe_3O_4 core [29,30]. Fe_3O_4@SiO_2-GO were determined using ICDD pdf # 01-076-5949 and also showed similar peaks and d-spacing at 2θ to Fe_3O_4 nanoparticles indicative of the stability of crystalline phase of Fe_3O_4 nanoparticles during covalently bonding of graphene oxide on Fe_3O_4@SiO_2-NH_2 [34]. However, the graphene oxide peak in Fe_3O_4@SiO_2-GO-PEA changed to a broad amorphous peak. This indicates that the structure of the graphene oxide was partially damaged during covalent bonding with Fe_3O_4@SiO_2-NH_2 [47]. Alternatively, the lack of a graphene oxide peak, despite the TEM evidence of it, may indicate the individual nanosheets are far apart thus no diffraction signal or a limited amount of graphene oxide relative to the nanocomposite.

3.1.4. Zeta potential results

Zeta potential measurements were done to determine the surface charge of the prepared graphene oxide, Fe_3O_4@SiO_2-NH_2, Fe_3O_4@SiO_2-GO and Fe_3O_4@SiO_2@GO-PEA at pH range between 2 and 12 (Fig. 7). The results show that the graphene oxide nanosheets were negatively charged with an average zeta potential value of −22.3 mV due to the oxygen functional groups on the surface of the nanomaterials [48]. Fe_3O_4@SiO_2-NH_2 was positively charged with a value of 2.4 mV due to the presence of the of amine group on the shell [34]. Upon covalently bonding of Fe_3O_4@SiO_2-NH_2 with graphene oxide, the average zeta potential was found to be −20.9 mV which was much lower compared to Fe_3O_4@SiO_2-NH_2. This demonstrates successful coating of graphene oxide on Fe_3O_4@SiO_2-NH_2 [34]. However, modification of Fe_3O_4@SiO_2-GO with 2-phenylethyl amine showed an increase in the average zeta potential to −6.9 mV. The isoelectric point increased when comparing Fe_3O_4@SiO_2-GO to Fe_3O_4@SiO_2-GO-PEA, and this was attributed to the presences of amine groups on the surface of Fe_3O_4@SiO_2-GO [49,50].

3.1.5. Textural properties of the nanomaterials

The N_2 adsorption −desorption isotherm, pore volume and the corresponding pore size distribution curve of Fe_3O_4, Fe_3O_4@SiO_2-NH_2 Fe_3O_4@SiO_2-GO and Fe_3O_4@SiO_2@GO-PEA are shown in Fig. 8 and the values summarised in Table 1. The isotherms were classified according to the IUPAC system as type IV [51]. For Fe_3O_4, and Fe_3O_4@SiO_2-NH_2 with a hysteresis loop of H1, which is often associated with materials that agglomerates or compacts of approximately spherical particles arranged in a uniform way. While Fe_3O_4@SiO_2-GO and Fe_3O_4@SiO_2@GO-PEA had a hysteresis loop of H3 which is associated with materials that aggregate of plate like particles forming slit like pores [51,52].

GO nanoparticle showed a BET surface area of 176 m^2/g (Table 1) which was much lower than the theoretical surface area (2630 m^2/g). This may be attributed to the agglomerations and restacking of GO layers during drying process and also due to unavoidable van der Waals force between each single sheet of GO [53,54]. The agglomeration GO can result in the partial overlapping and lowering the surface area of the bulk materials but still leaves many exposed surfaces [55]. On the other hand, it was observed that after coating Fe_3O_4 with SiO_2 and modifying with the amine group, there was an increase in specific surface area and pores volume due to the low specific weight of silica compared to that of magnetite [46]. On covalently bonding the GO with Fe_3O_4@SiO_2-NH_2, the BET surface area was 131 m^2/g which was further increased to 133 m^2/g on modification with PEA. This indicates the availability of active site for adsorption of the analyte [2]. The surface area of Fe_3O_4@SiO_2-GO-PEA was lower than GO due to the presence of Fe_3O_4@SiO_2-NH_2 on its surface. High pore sizes were observed in Fe_3O_4 and Fe_3O_4@SiO_2-NH_2 due to pores between nanoparticles [56]. However, both the Fe_3O_4@SiO_2-GO and Fe_3O_4@SiO_2-GO-PEA had a pore size ranging between 2 and 50 nm indicating the formation of a mesoporous material [51,57].

3.1.6. Analysis using a vibrating sample magnetometer (VSM)

The magnetic hysteresis loops of the prepared Fe_3O_4@SiO_2-NH_2, Fe_3O_4@SiO_2-GO and Fe_3O_4@SiO_2@GO-PEA were studied using VSM at 300 K as presented in Fig. 9. A separate permanent magnet (NdFeB) was used to investigate the response of the separation process of the nanoparticles from solution. The magnetic saturation (Ms) for Fe_3O_4, Fe_3O_4@SiO_2-NH_2, Fe_3O_4@SiO_2-GO and Fe_3O_4@SiO_2@GO-PEA were found to be 77 emu/g, 48 emu/g, 40 emu/g and 33 emu/g respectively. The decrease in magnetisation values was due to the presence of non-magnetic silica shell in the chemical bond Fe-O-Si and GO nano-sheets on the surface of Fe_3O_4 that disordered spin configuration, weakened magnetic moment of inner magnetic core, and diminished the inductive effect of the magnetic field [34,46,58].

The coercive field (Hc), and remnant magnetisation (Mr) were observed after removing the magnetic field and the results summarised in Table 2. The decrease in Hc in the nanocomposite as compared to that of the bare Fe_3O_4 magnetite is due to decrease in specific absorption rate (SAR) for silica coated samples which decreases the spin effects [58]. Furthermore, the silica shell encapsulating the magnetite particles effectively screens and thus decreases the magnetic dipole coupling interactions between neighbouring magnetic nanoparticles [58]. In addition, Fe_3O_4, Fe_3O_4@SiO_2−NH_2, Fe_3O_4@SiO_2-GO and Fe_3O_4@SiO_2@GO-PEA nanoparticles exhibited ferromagnetic properties [34]. However, despite the decrease in the magnetic properties, the

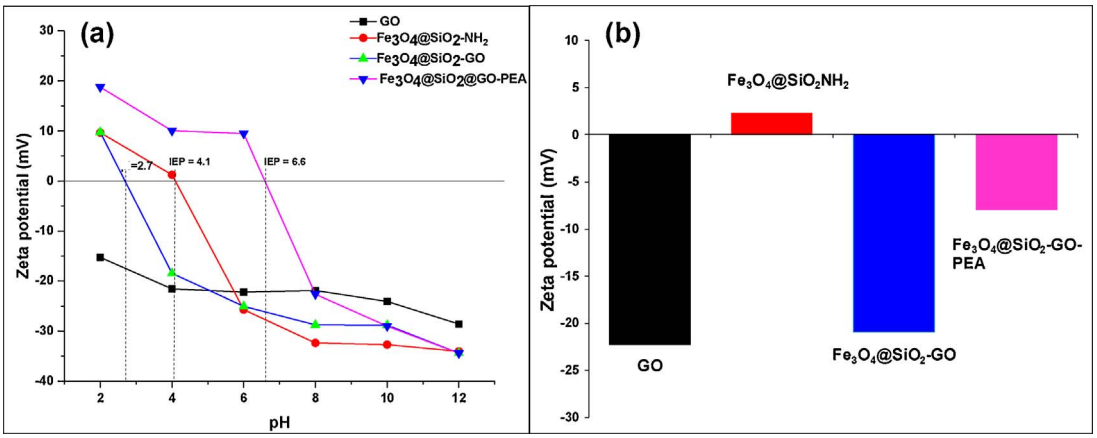

Fig. 7. Zeta potential and the isoelectric point (a) and average zeta potential (b) of graphene oxide (GO), Fe_3O_4@SiO_2-NH_2, Fe_3O_4@SiO_2-GO and Fe_3O_4@SiO_2-GO-PEA nanoparticles.

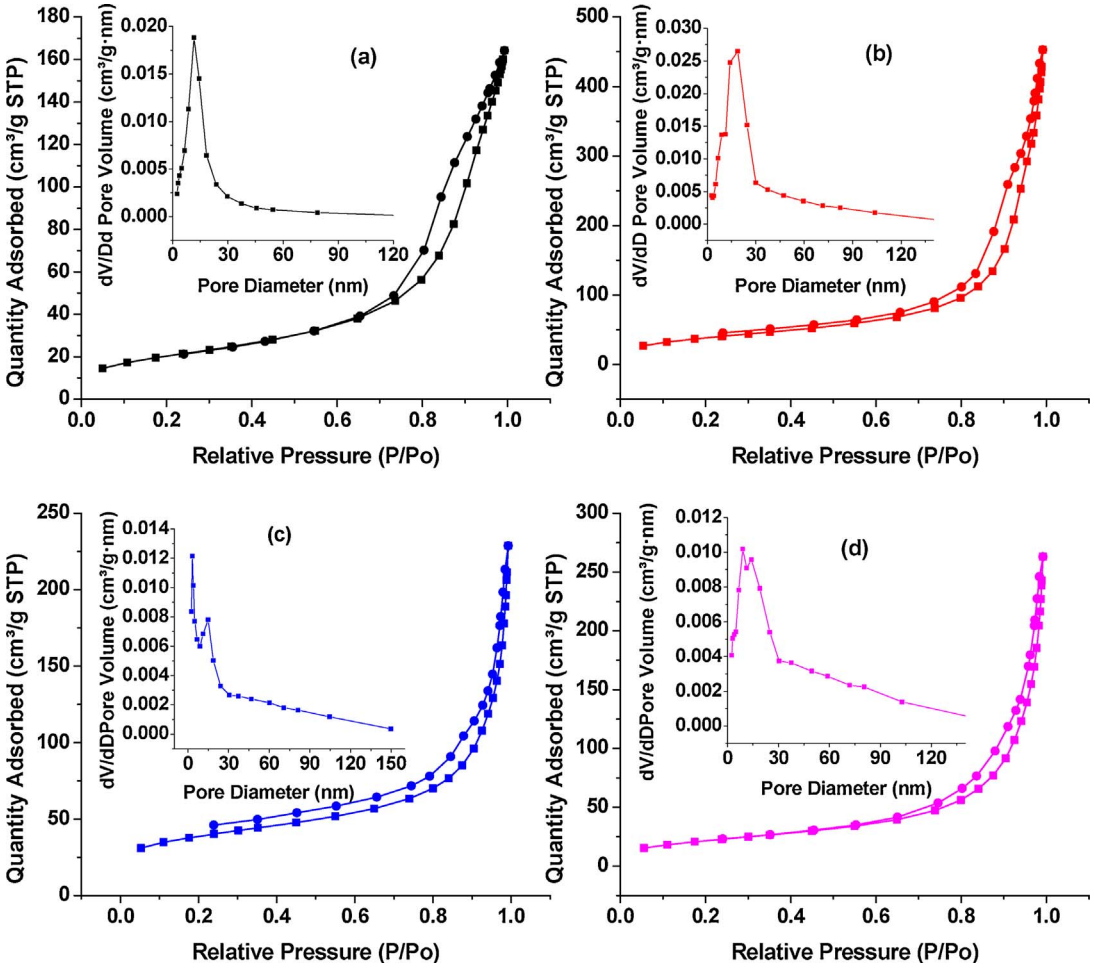

Fig. 8. Nitrogen adsorption–desorption of Fe_3O_4 (a) Fe_3O_4@SiO_2-NH_2 (b), Fe_3O_4@SiO_2-GO (c) and Fe_3O_4@SiO_2 @GO-PEA (d) nanoparticles.

nanoparticles can still be separated by using an external magnetic as can be seen in the inset of Fig. 9. The Fe_3O_4@SiO_2@GO-PEA nanocomposite can rapidly concentrate on the side of the glass vial on application of external magnet and dispersed in aqueous solution when the magnet is removed.

3.2. Sorption studies

The quantitative removal of chlorpyrifos, malathion and parathion mixture using the synthesized Fe_3O_4@SiO_2@GO-PEA nanocomposite was evaluated. Various factors which influence removal efficiency like adsorbent dosage, solution pH, adsorption time and pesticide concentration were optimized.

3.2.1. Effect of contact time

Contact time is an important factor in the removal of chlorpyrifos, malathion and parathion using Fe_3O_4@SiO_2@GO-PEA as an adsorbent. This was done at different adsorption time ranging from 1 to 60 min (n = 3) using a mechanical shaker at 25 °C. The other experimental conditions were kept constant i.e. OPPs concentration, 1 μg/L; pH 7;

Table 1
Characterization of Fe_3O_4, Fe_3O_4@SiO_2-NH_2, GO, Fe_3O_4@SiO_2-GO and Fe_3O_4@SiO_2-GO-PEA by nitrogen adsorption-desorption measurement.

Sample	BET Surface area (m^2/g)	BJH pore volume (cm^3/g)	Pore size (nm)
Fe_3O_4	73.0	0.22	11.6
Fe_3O_4@SiO_2-NH_2	100	0.32	18.5
GO	176	0.065	5.12
Fe_3O_4@SiO_2-GO	131	0.32	15.6
Fe_3O_4@SiO_2-GO-PEA	133	0.48	17.5

Table 2
Magnetic characteristics obtained from VSM analysis.

Sample	Ms (emu/g)	Mr (emu/g)	Hc (G)
Fe_3O_4	77	37	254
Fe_3O_4@SiO_2-NH_2	48	22	232
Fe_3O_4@SiO_2@GO	40	19	232
Fe_3O_4@SiO_2-GO-PEA	33	14	227

and adsorbent dosage, 10.0 mg. The percent removal rapidly increased with over 88%, 76% and 85% for chlorpyrifos, malathion and parathion pesticides respectively during the first 15 min as shown in Fig. 10a. There was no significant increase in percentage removal of the OPPs beyond the 15 min of contact time. This could be due to the establishment of an equilibrium between the available adsorption sites on the adsorbent and the sample solution, and due to the rapid mass transfer of analytes from the aqueous phase to the adsorbent during the first 15 min. Therefore 15 min was found to be the sufficient time to achieve the maximum percentage removal of the selected OPPs.

3.2.2. Effect of pH on adsorption

The pH of a solution is an important parameter affecting both the charge and stability in the removal of chlorpyrifos, malathion and parathion pesticides during the adsorption process. Hence the effect of the sample pH was investigated at different pH values ranging from 3 to 11 by adjusting the pH with 0.1 M HCl or 0.1 M NaOH while the other experimental conditions were kept constant (experiments were done in triplicates). The other experimental conditions were kept constant i.e. OPPs concentration, 1 µg/L; time; 15 min and adsorbent dosage, 10.0 mg. Results obtained are illustrated in Fig. 10b, and shows that there was no significant difference at different pH during the adsorption of the OPPs in water. This shows that the interaction of OPPs on the adsorbent through hydrogen bonding and π–π interaction were not affected by protonation and deprotonation during the pH adjustment. This is because the surface charge of Fe_3O_4@SiO_2@GO-PEA adsorbent is not significantly affected by changing of the pH solution due to the modification of graphene oxide with 2-phenylethyl amine (PEA). This was confirmed by zeta potential analysis done, (Fig. 7) which showed that the isoelectric point for Fe_3O_4@SiO_2@GO-PEA nanocomposites were 6.6. This may indicate that the variety of surface groups provide a range of favorable interactions across a wide range of pH values.

3.2.3. Effect adsorbent dosage

The adsorbent dosage is a key parameter to determine the quantitative removal of the selected analyte. The mass of the prepared Fe_3O_4@SiO_2@GO-PEA adsorbent was optimised within the range of 2–40 mg as illustrated in Fig. 10c. The other experimental conditions were kept constant i.e. OPPs concentration, 1 µg/L; pH 7; and time of 15 min (all experiments were done in triplicate). In the beginning, the percentage adsorption increased with increasing mass of the Fe_3O_4@SiO_2@GO-PEA adsorbent, this is due to the increased number of adsorption sites with increased adsorbent dosage. The quantitative removal of the three OPPs was obtained using 15 mg of the adsorbent with no significant change observed when the adsorbent dosage was increased above 15 mg. The maximum percentage removal for chlorpyrifos, malathion and parathion were 87%, 74% and 86% respectively. Therefore, 15.0 mg of the adsorbent was used for subsequent experiments.

3.2.4. Adsorption capacity

The adsorption capacity was determined using the optimum conditions obtained, where 15 mg of the Fe_3O_4@SiO_2@GO-PEA adsorbent was equilibrated with 10 mL of chlorpyrifos, malathion and parathion pesticides mix at a concentration range of 0.3 µg/mL–5 µg/mL (n = 3). Adsorption capacity was calculated using Eq. (2) and found to be 11.1 mg/g, 10.6 mg/g and 10.9 mg/g for chlorpyrifos, malathion and parathion respectively. However, since chlorpyrifos, malathion and parathion were analyzed as mix, the total adsorption capacity of the

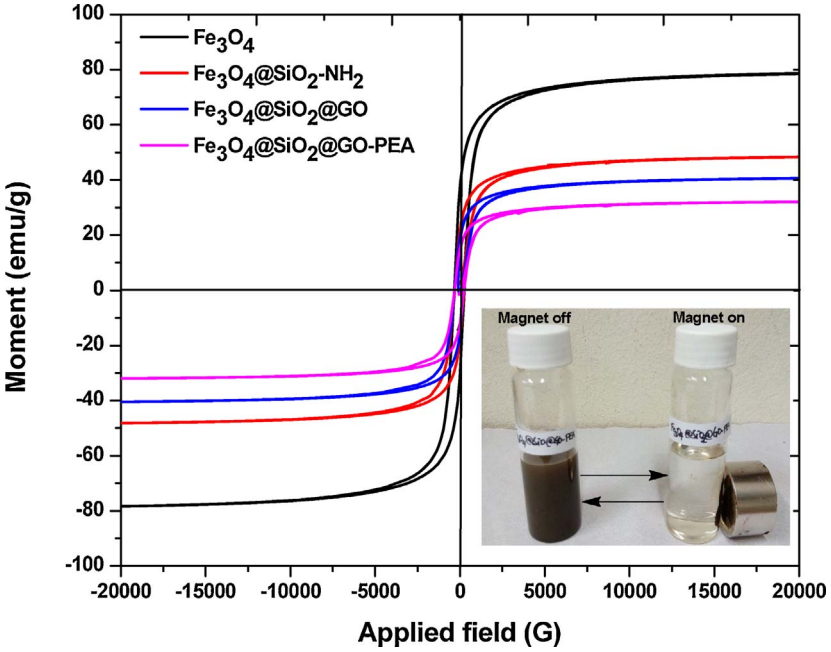

Fig. 9. Magnetic hysteresis loops and the insets showing the Fe_3O_4@SiO_2@GO-PEA in aqueous solution before and after magnetic separation by an external magnet.

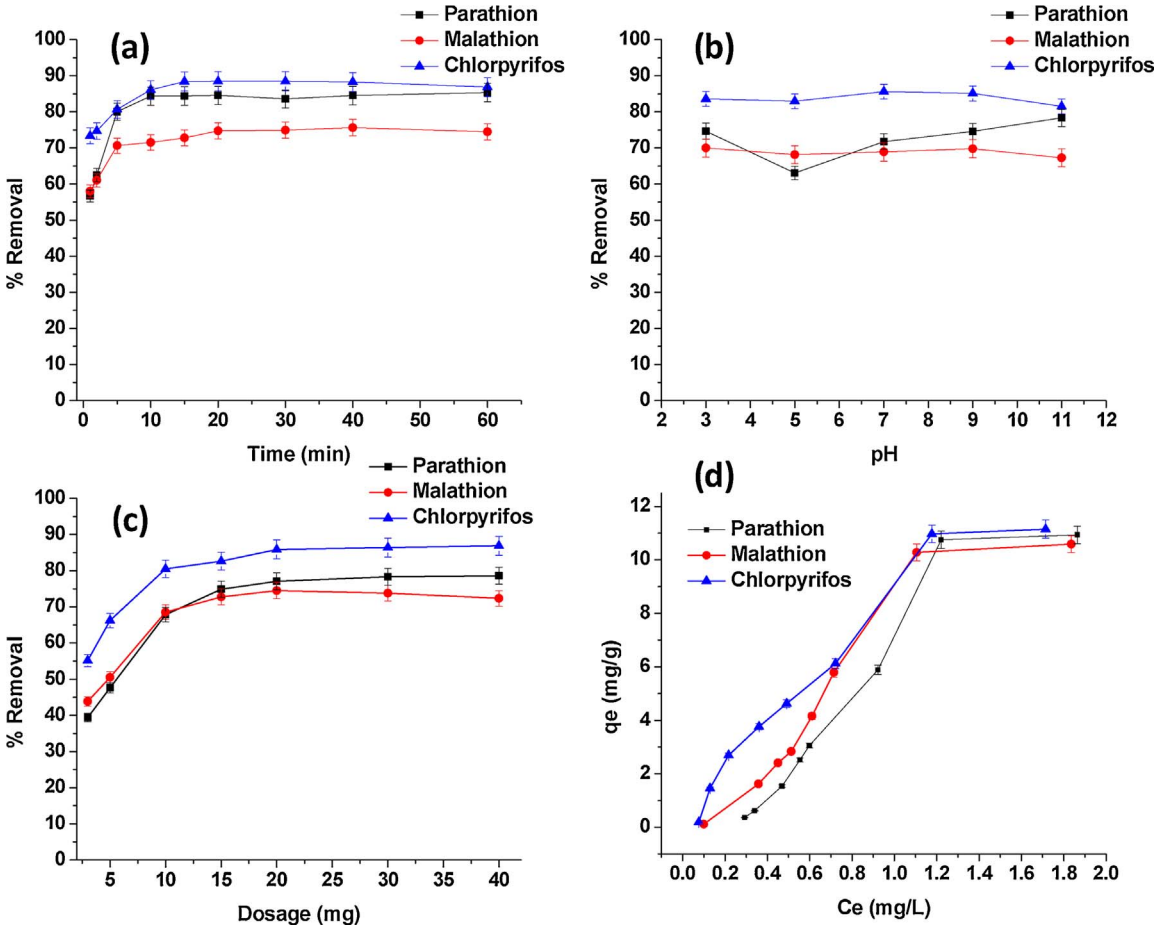

Fig. 10. Effect of contact time (a), pH (b), and adsorbent dosage (c) on% removal of selected OPPs. The adsorption capacity is shown in (d).

prepared Fe_3O_4@SiO_2@GO-PEA adsorbent was 32.6 mg/g. Fig. 10d illustrates that the adsorption capacity of chlorpyrifos, malathion and parathion on Fe_3O_4@SiO_2@GO-PEA increased upon increasing the concentration until the adsorbent sites were saturated. No significant difference was observed in the adsorption of the adsorbate indicating that the adsorbent had a fixed number of binding sites for the adsorption of chlorpyrifos, malathion and parathion pesticides [59]. High adsorption capacity of chlorpyrifos, malathion and parathion pesticides on Fe_3O_4@SiO_2@GO-PEA adsorbent indicates that the molecules could penetrate through the pores or be adsorbed on the surface of the adsorbent via physical forces [60]. Previous studies have suggested that the phenyl ring and charged groups on graphene oxide nanocomposites participate in the sorption process [2]. From our FTIR results, amine groups, carbonyl groups, and OH groups are present on the sorbent, and will interact with the OPPs via hydrogen bonding. In addition, the sorbent has phenyl rings throughout the structure, which will result in π–π interaction with the OPPs, especially with chlorpyrifos and parathion. Thus, chlorpyrifos and parathion can interact via hydrogen bonding and π–π interactions, whereas malathion is most likely dominated by hydrogen bonding alone. This can tentatively explain the order of the sorption capacities, which were chlorpyrifos, parathion, and malathion.

3.2.5. Adsorption isotherms

Adsorption isotherms are important in ascertaining how solutes interact with adsorbents and feasibility of different adsorption processes on adsorbing a particular adsorbate. They are also useful for investigating the distribution of adsorption molecules between liquid and solid phase when the state of equilibrium is achieved [4,29]. To understand how the functional groups on the Fe_3O_4@SiO_2@GO-PEA adsorbent affect the adsorption process, adsorption isotherm of chlorpyrifos, malathion and parathion pesticides were conducted. The equations used to model the adsorption isotherms were Langmuir [25,26,61], Freundlich [25–27,61], Temkin [25], Dubinin–Radushkevich (D-R) [4,61,62], Sips [63], and Redlich and Peterson [61,63]. The non-linear forms for the applied models are as follows;

Langmuirequation $$q_e = \frac{Q^0_{max} K_L C_e}{1 + K_L C_e} \quad (5)$$

Freundlichequation $$q_e = K_F C_e^n \quad (6)$$

Temkinequation $$q_e = \frac{RT}{b_T} \ln A_T C_e \quad (7)$$

Dubinin-Radushkevichequation $$q_e = q_{DR} e^{-K_{DT}\varepsilon^2} \quad (8)$$

$$\varepsilon = RT \ln 1 + \frac{1}{C_e} \quad (9)$$

$$E = \frac{1}{\sqrt{-2K_{DR}}} \quad (10)$$

Sipsequation $$q_e = \frac{K_s C_e^{bs}}{1 + a_s C_e^{bs}} \quad (11)$$

RedlichandPetersonequation $$q_e = \frac{K_R C_e}{1 + a_R C_e^{bR}} \quad (12)$$

The common parameters, q_e (mg/g) and C_e (mg/L), are the equilibrium adsorption capacity and equilibrium concentration of adsorbate solution respectively. The constants K_L (L/mg) and Q^{00}_{max} (mg/g) are the Langmuir's constant and maximum monolayer adsorption capacity. K_F (mg/g)/(mg/L)^n and n (dimensionless) are Freundlich constant

indicative of the relative adsorption capacity of the adsorbent and intensity of the adsorption and varies with surface heterogeneity respectively. The constant A_T (L/mg) is the Temkin constant and b (kJ/moL) is the heat of adsorption. The constant K_{DR} (moL^2/kJ^2) is the DKR model constant related to mean free energy of adsorption per mole of adsorbent, T (in Kelvin) is temperature, R (8.314 J/mol/K) is the universal gas constant and ε is the Polanyi potential. Finally, E is the mean free energy of adsorption (kJ/moL). The parameters in the Sips equation include the Sips model isotherm constant (K_s (L/mg)), the Sips model constant (a_s (L/mg)), and the Sips model exponent (b_s). The Redlich Peterson constants are defined by K_R and a_R, and b_R is a dimensionless exponent that must lie between 1 and 0.

The values of the isotherms parameters were calculated using non linear methods utlising the 'solver add-in' in Excel™ 2013. The methods were adapted from the references [61,64], and the R^2 (coefficient of determination), and χ^2 (chi-squared) values were determined using Eqs. (13) and (14).

$$\textbf{Coefficientofdetermination}\quad R^2 = 1 - \frac{\sum\left(q_{e.exp} - q_{e,cal}\right)^2}{\sum\left(q_{e,exp} - q_{e,mean}\right)^2} \tag{13}$$

$$\textbf{Chi} - \textbf{squaredequations}\quad \chi^2 = \sum \frac{\left(q_{e,exp} - q_{e,cal}\right)^2}{q_{e,cal}} \tag{14}$$

An initial qualitive assement on how well the models fit the experimental data were done graphically, and the results are presented in Fig. 11. From the figure, the Langmuir, Freundlich, Temkin, and the Redlich and Peterson (labelled R-P in Fig. 11) models fit the experimental data relatively poorly. In contrast the Dubinin–Radushkevich (labelled D-R in Fig. 11) and Sips model seem to provide an excellent fit to the data.

The key values extracted from the non-linear fitting of the data to the various equations are presented in Table 3. The Langmuir and Freundlich isotherms have R^2 values above 0.9 for Parathion and Chlorpyrifos, and a relatively low value for Malathion. The Temkin model shows R^2 values above 0.9 for all three OPPs; however, the relatively large b (kJ/moL) values (heats of adsorption) suggest the model

Table 3
Isotherm parameters for the adsorption of Parathion, Malathion and Chlorpyrifos on Fe_3O_4@SiO_2@GO-PEA.

Isotherm Model	Isotherm Parameter	Parathion	Malathion	Chlorpyrifos
Langmuir	Q^0_{max} (mg/g)	135	61.9	25.6
	K_L (L/mg)	0.0435	0.124	0.510
	R^2	0.924	0.889	0.971
	χ^2	0.224	0.347	0.0959
Freundlich	K_F (mg/g)/(mg/L)^n	5.23	6.64	8.18
	n	1.23	0.951	0.749
	R^2	0.966	0.881	0.954
	χ^2	0.108	0.378	0.150
Temkin	b(kJ/moL)	425	610	657
	A_T (L/mg)	3.10	5.93	10.4
	R^2	0.985	0.921	0.976
	χ^2	0.108	0.668	0.218
Dubinin–Radushkevich	q_{DR} (mg/g)	14.9	14.6	13.1
	K_{DR} (mol^2/kJ^2)	0.274	0.205	0.109
	E (kJ/mol)	1.35	1.56	2.14
	R^2	0.999	0.963	0.969
	χ^2	0.00221	0.121	0.107
Sips	K_s (L/mg)	13.8	47.7	24.2
	a_s (L/mg)	1.07	4.24	1.63
	b_s	2.60	3.65	1.49
	R^2	0.999	0.995	0.993
	χ^2	0.00471	0.0400	0.0655
Redlich and Peterson	a_R (L/mg)	0.00	0.000105	0.0324
	K_R (L/g)	5.57	7.75	10.0
	b_R	13.3	13.3	5.22
	R^2	0.971	0.972	0.998
	χ^2	1.33	1.51	0.148

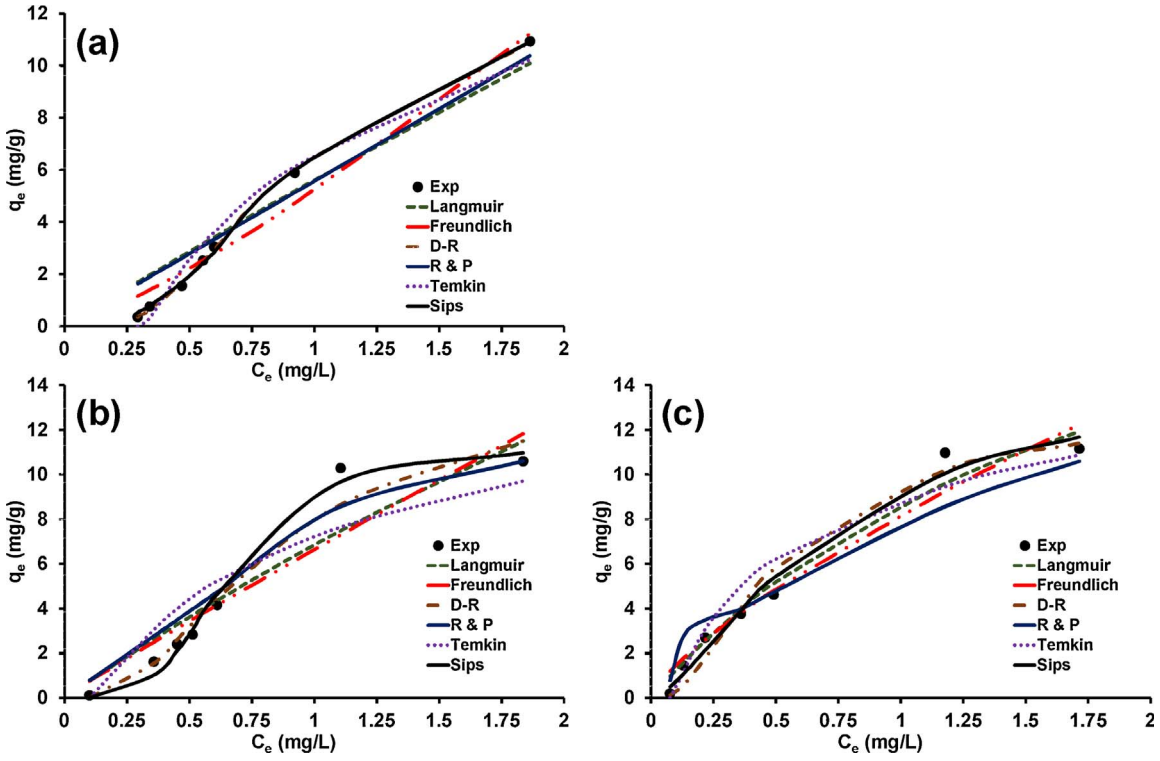

Fig. 11. Graphical fit, to the experimental data, of the various isotherm models for parathion (a), Malathion (b), and chlorpyrifos (c).

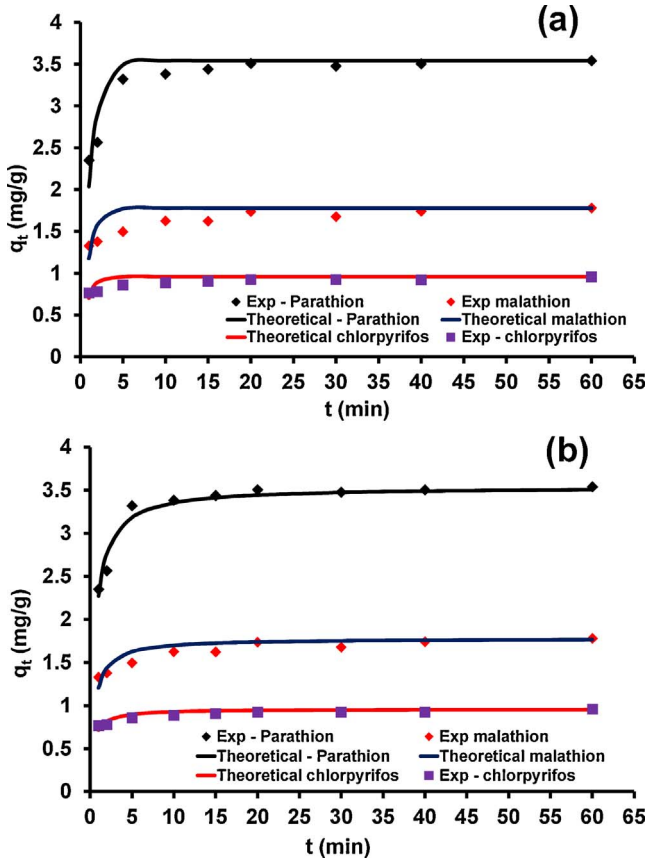

Fig. 12. Pseudo-first-order kinetics (a) and Pseudo-second-order kinetics (b) for adsorption of chlorpyrifos, malathion, and parathion.

most likely cannot be used to explain the data. The results obtained further show that the Redlich and Peterson equation is not suitable for describing the sorption process for all three OPPs. This is due to the b_R exponent having a value above 1 [61], and despite obtaining R^2 values above 0.9 (and relatively small χ^2) for each OPP and further supporting the relatively poor graphical fit to the experimental data (Fig. 12).

The Dubinin–Radushkevich isotherm models showed a good fit to the experimental data, with R^2 values above 0.9 for all 3 OPPs. The adsorption energy (E) for Parathion, Malathion and Chlorpyrifos were 1.352, 1.562, and 2.139 kJ/mol respectively, indicating a physical adsorption process on Fe_3O_4@SiO_2@GO-PEA nano-composite. This implies that the adsorption process occurred onto both homogeneous and heterogeneous surfaces [61]. This concurs with the observations from the FTIR analysis, which showed that various functional groups are responsible for π–π and hydrogen bonding interactions.

Overall, the Sips equation provided the best fit to the data, and can be used to describe the sorption process for all three OPPs, as per the graphical analysis, and the values presnted in Table 3. The Sips model exponent (b_s), is associated with the heterogeneity of the sorption [63,65–68] process, and values above 1 demonstrate a heterogeneous system. All three pesticides had values above 1, clearly indicating the heterogeneity of the process. The Sips isotherm can be used to describe sorption onto heterogeneous surfaces [63,65–68], and from the characterization of the materials, the nanocomposite consists of various functional groups that can account for the heterogeneous process associated with the sorption of the pesticides. These include functional groups responsible for van der Waals forces, hydrogen bonding, and π–π interactions. These various functional groups may explain why the Sips model provides the best fit to the data.

The Sips model isotherm constant (K_s (L/mg)) is indicative of the adsorption affinity of the adsorbates to the absorbents [63,65–68]. From the data, malathion (47.7) > chlorpyrifos (24.2) > parathion (13.8) in terms of affinity for the sorbent. It is not clear why the pesticides follow such an order, but the malathion molecule has more electronegative atoms and the structure maybe relatively more flexible and allow for more favorable reconfigurations and interactions with the surface of the adsorbent. The difference between chlorpyrifos and parathion could be due to the greater number of electronegative atoms on chlorpyrifos. However, further investigations using computational work is needed to gain greater insights in terms of the sorption mechanisms.

3.2.6. Adsorption kinetics

To ascertain the kinetic mechanism and potential rate of adsorption of chlorpyrifos, malathion and parathion on Fe_3O_4@SiO_2@GO-PEA adsorbent, data from the effect of time experiment were fitted into pseudo-first-order and pseudo-second-order kinetic models [61] as shown in Eqs. (17) and (18).

$$\textbf{Pseudo} - \textbf{first} - \textbf{order}: \quad q_t = q_e(1 - e^{-k_1 t}) \tag{17}$$

$$\textbf{Pseudosecond} - \textbf{order}: \quad q_t = \frac{q_e^2 k_2 t}{1 + k_2 q_e t} \tag{18}$$

Where K_1 is the pseudo first-order rate constant, K_2 is the pseudo-second-order rate constant qe (mg/g), q_t (mg/g) are equilibrium adsorption capacity and adsorption capacity mol/g at a given time (t) respectively. Nonlinear fitting of the experimental data was done using the 'solver add-in' in Excel™ 2013, and adapting methods outlined in the references [61,64], and are presented in Fig. 12.

The rate constants, coefficients of determination (R^2), and chi-squared values (χ^2) are summarized in Table 4. The data shows that the kinetic processes for the sorption of the three OPPs onto Fe3O4@SiO2@GO-PEA favored pseudo second-order kinetics. Similar observations were made by Kamboh and coworker where they used Calix-EPPTMS-MS in the removal of chlorpyrifos and diazinon [4]. Gupta and coworkers also had the same observation when they used carbon slurry in the removal of endosulfan and methoxychlor from aqueous solution [69].

3.3. Recycling and reuse of the adsorbent

To examine the reusability of the Fe_3O_4@SiO_2@GO-PEA adsorbent, the used adsorbent was washed twice with 2 mL of acetone, and then with 2 mL of distilled water with a vortex mixer for approximately 2 min. The adsorbent was collected using a magnetic and reused for the next analysis run. In each analysis run, 1 µg/mL of OPPs sample solution was tested according to the procedure described in Section 2.6 under optimal conditions. The percentage recovery of the chlorpyrifos, parathion and malathion pesticides after ten cycles of adsorption–desorption process were in the range of 89%-100% (Fig. 13), with RSD between 4 and 8%. Thus, this indicates that the synthesized Fe_3O_4@SiO_2@GO-PEA nanocomposite could be reused up to 10 times without a significant loss of adsorption. Therefore, the proposed material possesses acceptable reusability.

Iron oxide nanoparticles have been investigated for decades as

Table 4
Comparison of Pseudo first-order and second-order kinetics constants for the adsorption of chlorpyrifos, malathion and parathion using Fe_3O_4@SiO_2@GO-PEA.

OPPs	Pseudo first order kinetics			Pseudo second order kinetics		
	K_1	R^2	χ^2	K_2	R^2	χ^2
Parathion	0.856	0.824	0.00950	0.506	0.955	0.00251
Malathion	1.09	0.0512	0.0131	1.19	0.729	0.00387
Chlorpyrifos	1.32	−0.0546	0.00457	3.03	0.718	0.00125

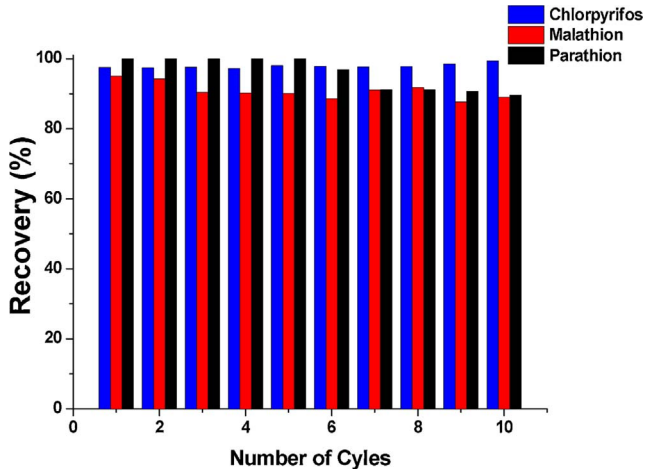

Fig. 13. Recycling and reuse of the Fe_3O_4@SiO_2@GO-PEA adsorbent in the removal of chlorpyrifos, malathion and parathion mix from aqueous solution.

environmental remediation systems; including, usage for degradation and/or removal of organic compounds from aqueous systems [70]. The addition of a silica coating on the iron oxide nanoparticles prevents direct interaction between the active iron oxide core and the selected pesticides used in the current study. The covalently bonded graphene oxide and the 2-phenylethyl amine molecule provides a large surface area and wide range of functional groups (various carbonyl and amine based) that are effective in the adsorption and extraction of the selected pesticides. In addition, the pH studies (Fig. 10(b)) highlighted the effectiveness of the material across a wide range of pH ranges. Thus the silica coated iron oxide core allows for easy separation of the material, and the synergy between the graphene oxide, and 2-phenylethyl amine molecule allows for an effective sorbent that can be effectively used for 10 cycles.

3.4. Comparison of pesticide extraction with reported literature

A comparison of the Sips isotherm parameters for the pesticides sorbed on Fe_3O_4@SiO_2@GO-PEA adsorbent with other adsorbents reported in the literature are summarised in Table 5.

The Fe_3O_4@SiO_2@GO-PEA nanomaterial has a higher Sips isotherm constant K_s (L/mg), than most other materials. Ordered mesoporous materials have a higher affinity for the target analyte, and can be attributed to the large surface area (888 vs 133 m^2/g in this study) and surface properties. Carbon nanotubes have values a bit larger than the Fe_3O_4@SiO_2@GO-PEA nanomaterial affinity for parathion, but much smaller when compared to the other two pesticides on the graphene oxide nanocomposite. In general the sorption process depends on several factors; such as, pH, concentration, dosage, surface area, surface properties of the sorbent, time, and temperature. Thus comparing the nanocomposite in this study, with various materials and adsorbates from the literature is most likely more qualitative than quantitative.

3.5. Real sample analysis

To assess the field applicability of the developed Fe_3O_4@SiO_2@GO-PEA as an adsorbent, chlorpyrifos, malathion, and parathion were extracted from environmental water samples collected from Vaal River and Vaal Dam in Gauteng province in South Africa. Water samples were analyzed before spiking to ascertain the presence or absence of chlorpyrifos, malathion, and parathion. The results showed that chlorpyrifos, malathion and parathion pesticides in Vaal river and Vaal Dam were below the detection limit. Hence to verify the accuracy of the method, river water and dam water were spiked with 0.5 μg/mL of OPPs mix and then analysed at optimum conditions obtained. The recoveries obtained were greater than 86.9% with intraday%RSD of less than 9.6% for Vaal river water samples while in Vaal dam water samples, the recovery was greater than 90.1% with intraday%RSD less than 8.2% for the OPPs. These% recovery values obtained are within the range stipulated by the U.S. Environmental Protection Agency (EPA) which is from 70% to

Table 5
Comparison of Sips isotherm parameters with reported literature.

Adsorbent	Adsorbate	Dosage (mg/mL)	pH	Temp (°C)	a_s (L/mg)	K_s (L/mg)	b_s	Ref
Ordered Mesoporous Carbon	Hexachlorobenzene	0.2	N/A	25	N/A	870	1.05	[67]
Glycerol-based carbon materials	Tetracycline	2.4	6.3	30	N/A	0.06	1	[71]
Glycerol-based carbon materials	Flumequine	2.4	6.3	30	N/A	0.37	0	[71]
Carbon Aerogel	Caffeine	2.4	N/A	30	N/A	2.96×10^{-6}	4.6	[65]
Carbon Aerogel	Diclofenac	2.4	N/A	30	N/A	1.30×10^{-6}	2.8	[65]
granular activated carbon	(2,4-dichlorophenoxy) acetic acid	0.2	N/A	25	N/A	0.191	1.617	[72]
granular activated carbon	(RS)-2-(2,4-dichlorophenoxy) propionic acid	0.2	N/A	25	N/A	0.111	1.554	[72]
granular activated carbon	4-(2,4-dichlorophenoxy) butyric acid	0.2	N/A	25	N/A	0.112	1.515	[72]
granular activated carbon	(2,4,5-trichlorophenoxy) acetic acid	0.2	N/A	25	N/A	0.154	1.451	[72]
granular activated carbon	(4-chloro-2-methylphenoxy) acetic acid	0.2	N/A	25	N/A	0.275	1.982	[72]
Powdered activated carbon	(2,4-dichlorophenoxy) acetic acid	0.2	N/A	25	N/A	0.075	1.463	[72]
Powdered activated carbon	(RS)-2-(2,4-dichlorophenoxy) propionic acid	0.2	N/A	25	N/A	0.261	1.357	[72]
Powdered activated carbon	4-(2,4-dichlorophenoxy) butyric acid	0.2	N/A	25	N/A	0.18	1.367	[72]
Powdered activated carbon	(2,4,5-trichlorophenoxy) acetic acid	0.2	N/A	25	N/A	0.259	1.698	[72]
Powdered activated carbon	(4-chloro-2-methylphenoxy) acetic acid	0.2	N/A	25	N/A	0.578	1.41	[72]
switchgrass biochar	metribuzin	1	2	25	0.002	1.795 (L/g)	0.76	[73]
Magnetic switchgrass biochar	metribuzin	1	2	25	0.005	0.765 (L/g)	1.026	[73]
Multiwalled Carbon Nanotubes	chloroform	0.25	5	25	3.213	18.957	2.35	[66]
Multiwalled Carbon Nanotubes	dichlorobromomethane	0.25	5	25	3.431	18.553	1.68	[66]
Multiwalled Carbon Nanotubes	dibromochloromethane	0.25	5	25	3.068	15.722	1.7	[66]
Multiwalled Carbon Nanotubes	bromoform	0.25	5	25	2.075	9.964	1.42	[66]
Charred Palm Kernal shells	Atenolol	1	7	25	N/A	4.34	0.88	[68]
Charred Palm Kernal shells	Acebutolol	1	7	25	N/A	1.73	0.37	[68]
Charred Palm Kernal shells	Carbamazepine	1	7	25	N/A	0.45	0.81	[68]
Fe_3O_4@SiO_2@GO-PEA	Parathion	1.5	7	25	1.07	13.8	2.6	Current study
Fe_3O_4@SiO_2@GO-PEA	Malathion	1.5	7	25	4.24	47.7	3.65	Current study
Fe_3O_4@SiO_2@GO-PEA	Chlorpyrifos	1.5	7	25	1.63	24.2	1.49	Current study

130%, with a maximum relative standard deviation of 30% [74]. Therefore, the prepared Fe_3O_4@SiO_2@GO-PEA nanoparticle having high adsorption capacity can be applied in MSPE techniques for the analysis of pesticides within real world samples.

4. Conclusions

The FTIR analysis showed shifts in the characteristic Fe—O bond vibrations after coating with silica, which indicated that the silica coating had intimately bonded with the iron oxide nanoparticles. Furthermore, each nanocomposite showed a broad FTIR peak due to sorption of water which is indicative of a surface favorable to hydrogen bonding. From the TEM analysis, the iron oxide particles were observed to be spherical, and on coating with silica a separate coating was observed, with an average thickness of 9.9 nm. The TEM observations confirmed that the silica had coated the iron oxide nanoparticles, as was inferred from the FTIR results. The TEM analysis also showed the characteristic sheet-like structure of the graphene oxide before and after attachment to the silica coated iron oxide nanoparticles. XRD analysis confirmed the formation of the graphene oxide, iron oxide nanoparticles, silica iron oxide nanoparticles, and indicative identification of the nanocomposites. From the FTIR, XRD, and TEM analysis, the successful synthesis of the nanomaterials and nanocomposites was confirmed.

The Fe_3O_4@SiO_2@GO-PEA adsorbent showed fast magnetic separation from the sample solution by using an external magnet, low adsorption time (15 min) and required no adjustments to the pH during adsorption. The maximum adsorption capacity (q_e) of Fe_3O_4@SiO_2@GO-PEA at optimum conditions for chlorpyrifos, malathion and parathion mix were 32.6 mg/g. The sips isotherm model best described the experimental data, and this was attributed the adsorbent's high surface area and the interaction between Fe_3O_4@SiO_2@GO-PEA and the pesticides. The heterogeneity of the process was attributed to the various surface groups on the nanocomposite, and the resulting hydrogen bonding and π–π interaction interactions between the nanocomposite and the electronegative atoms (P, N and S) on the pesticides. The adsorption kinetic investigations of chlorpyrifos, malathion and parathion were best described by pseudo-second-order kinetic models. The reusability data, magnetic properties, sorption and kinetic data may provide some insights in designing and implementing suitable processes for water treatment, extraction of target analytes for analysis, or improving the efficiency of existing systems.

Testing of the nanocomposite on real world studies demonstrated that the Fe_3O_4@SiO_2@GO-PEA can be used as a potential MSPE for the analysis of pesticides from environmental matrices.

Acknowledgements

The authors are grateful to the Faculty of Science, University of Johannesburg and National Research Foundation (NRF), South Africa for financial support. CJS and AREP would like to acknowledge that this work was based on the research supported in part by NRF Grant Numbers: 88080. We would also like to acknowledge the valuable assistance of Dr. Ndinteh (Applied chemistry) and Mark Peterson (LECO Company) with the GC–MS analysis.

References

[1] M. Šťastný, V. Štengl, J. Henych, J. Tolasz, P. Vomáčka, J. Ederer, Mesoporous manganese oxide for the degradation of organophosphates pesticides, J. Mater. Sci 51 (2016) 2634–2642.
[2] S. Mahpishanian, H. Sereshti, M. Baghdadi, Superparamagnetic core-shells anchored onto graphene oxide grafted with phenylethyl amine as a nano-adsorbent for extractionand enrichment of organophosphorus pesticides from fruit, vegetable and water samples, J. Chromatogr. A 1406 (2015) 48–58.
[3] Y. Merdassa, J.F. Liu, N. Megersa, Development of a one-step microwave-assisted extraction method for simultaneous determination of organophosphorus pesticides and fungicides in soils by gas chromatography-mass spectrometry, Talanta 114 (2013) 227–234.
[4] M.A. Kamboh, W.A.W. Ibrahim, H.R. Nodeh, M.M. Sanagi, S.T.H. Sherazi, The removal of organophosphorus pesticides from water using a new amino-substituted calixarene-based magnetic sporopollenin, New J. Chem. 40 (2016) 3130–3138.
[5] H. Heidari, H. Razmi, Multi-response optimization of magnetic solid phase extraction based on carbon coated Fe_3O_4 nanoparticles using desirability function approach for the determination of the organophosphorus pesticides in aquatic samples by HPLC–UV, Talanta 99 (2012) 13–21.
[6] S. Jin, Z. Xu, J. Chen, X. Liang, Y. Wu, X. Qian, Determination of organophosphate and carbamate pesticides based on enzyme inhibition using a pH-sensitive fluorescence probe, Anal. Chim. Acta 523 (2004) 117–123.
[7] H. Thiermann, L. Szinicz, P. Eyer, N. Felgenhauer, T. Zilker, F. Worek, Lessons to be learnt from organophosphorus pesticide poisoning for the treatment of nerve agent poisoning, Toxicology 233 (2007) 145–154.
[8] M. Jokanović, Medical treatment of acute poisoning with organophosphorus and carbamate pesticides, Toxicol. Lett. 190 (2009) 107–115.
[9] W.A.W. Ibrahim, H.R. Nodeh, H.Y. Aboul-Enein, M.M. Sanagi, Magnetic solid-phase extraction based on modified ferum oxides for enrichment preconcentration, and isolation of pesticides and selected pollutants, Crit. Rev. Anal. Chem. 45 (2015) 270–287.
[10] C. Sasikala, S. Jiwal, P. Rout, M. Ramya, Biodegradation of chlorpyrifos by bacterial consortium isolated from agriculture soil, World J. Microbiol. Biotechnol. 28 (2012) 1301–1308.
[11] S. Mahpishanian, H. Sereshti, Graphene oxide-based dispersive micro-solid phase extraction for separation and preconcentration of nicotine from biological and environmental water samples followed by gas chromatography-flame ionization detection, Talanta 130 (2014) 71–77.
[12] L. Wu, Y. Song, M. Hu, H. Zhang, A. Yu, C. Yu, Q. Ma, Z. Wang, Application of magnetic solvent bar liquid-phase microextraction for determination of organophosphorus pesticides in fruit juice samples by gas chromatography mass spectrometry, Food Chem. 176 (2015) 197–204.
[13] X. Wang, B. Liu, Q. Lu, Q. Qu, Graphene-based materials: fabrication and application for adsorption in analytical chemistry, J. Chromatogr. A 1362 (2014) 1–15.
[14] S. Chinthakindi, A. Purohit, V. Singh, V. Tak, D.R. Goud, D.K. Dubey, D. Pardasani, Iron oxide functionalized graphene nano-composite for dispersive solid phase extraction of chemical warfare agents from aqueous samples, J. Chromatogr. A 1394 (2015) 9–17.
[15] F. Perreault, A. Fonseca de Faria, M. Elimelech, Environmental applications of graphene-based nanomaterials, Chem. Soc. Rev. 44 (2015) 5861–5896.
[16] N. Li, J. Chen, Y.-P. Shi, Magnetic graphene solid-phase extraction for the determination of carbamate pesticides in tomatoes coupled with high performance liquid chromatography, Talanta 141 (2015) 212–219.
[17] X. Wang, H. Wang, M. Lu, X. Ma, P. Huang, X. Lu, X. Du, 3-D graphene-supported mesoporous SiO_2 @Fe_3O_4 composites for the analysis of pesticides in aqueous samples by magnetic solid-phase extraction with high-performance liquid chromatography, J. Sep. Sci. 39 (2016) 1734–1741.
[18] Q. Wu, G. Zhao, C. Feng, C. Wang, Z. Wang, Preparation of a graphene-based magnetic nanocomposite for the extraction of carbamate pesticides from environmental water samples, J. Chromatogr. A 1218 (2011) 7936–7942.
[19] D. Huang, C. Deng, X. Zhang, Functionalized magnetic nanomaterials as solid-phase extraction adsorbents for organic pollutants in environmental analysis, Anal. Methods 6 (2014) 7130–7141.
[20] M. Arvand, M. Hassannezhad, Magnetic core-shell Fe_3O_4@SiO_2/MWCNT nanocomposite modified carbon paste electrode for amplified electrochemical sensing of uric acid, Mater. Sci. Eng., C 36 (2014) 160–167.
[21] T.K.H. Ta, M.-T. Trinh, N.V. Long, T.T.M. Nguyen, T.L.T. Nguyen, T.L. Thuoc, B.T. Phan, D. Mott, S. Maenosono, H. Tran-Van, V.H. Le, Synthesis and surface functionalization of Fe_3O_4-SiO_2 core-shell nanoparticles with 3-glycidoxypropyltrimethoxysilane and 1,1′-carbonyldiimidazole for bio-applications, Colloids Surf., A 504 (2016) 376–383.
[22] K.C. de Souza, G.F. Andrade, I. Vasconcelos, I.M. de Oliveira Viana, C. Fernandes, E.M.B. de Sousa, Magnetic solid-phase extraction based on mesoporous silica-coated magnetic nanoparticles for analysis of oral antidiabetic drugs in human plasma, Mater. Sci. Eng., C 40 (2014) 275–280.
[23] D.C. Marcano, D.V. Kosynkin, J.M. Berlin, A. Sinitskii, Z. Sun, A. Slesarev, L.B. Alemany, W. Lu, J.M. Tour, Improved synthesis of graphene oxide, ACS Nano 4 (2010) 4806–4814.
[24] J. Zou, Y.-G. Peng, Y.-Y. Tang, A facile bi-phase synthesis of Fe_3O_4@SiO_2 core-shell nanoparticles with tunable film thicknesses, RSC Adv. 4 (2014) 9693.
[25] R. Sharma, P. Saini, Graphene-based composites and hybrids for water purification applications, in: M. Aliofkhazraei (Ed.), Diamond and Carbon Composites and Nanocomposites. InTech, Rijeka, 2016(Ch. 02).
[26] L. Zhou, S. Pan, X. Chen, Y. Zhao, B. Zou, M. Jin, Kinetics and thermodynamics studies of pentachlorophenol adsorption on covalently functionalized Fe_3O_4@SiO_2-MWCNTs core-shell magnetic microspheres, Chem. Eng. J. 257 (2014) 10–19.
[27] M.B. Desta, Batch sorption experiments: langmuir and freundlich isotherm studies for the adsorption of textile metal ions onto teff straw (*Eragrostis tef*) agricultural waste, J. Thermodyn. 2013 (2013), http://dx.doi.org/10.1155/2013/375830 (Article ID 375830, 6 pages).
[28] T. Yang, L.-h. Liu, J.-w. Liu, M.-L. Chen, J.-H. Wang, Cyanobacterium metallothionein decorated graphene oxide nanosheets for highly selective adsorption of ultra-trace cadmium, J. Mater. Chem. 22 (2012) 21909–21916.
[29] H.R. Nodeh, W.A.W. Ibrahim, M.A. Kamboh, M.M. Sanagi, Dispersive graphene-based silica coated magnetic nanoparticles as a new adsorbent for preconcentration of chlorinated pesticides from environmental water, RSC Adv. 5 (2015) 76424–76434.

[30] H.R. Nodeh, W.A.W. Ibrahim, I. Ali, M.M. Sanagi, Development of magnetic graphene oxide adsorbent for the removal and preconcentration of As (III) and As (V) species from environmental water samples, Environ. Sci. Pollut. Res. 23 (2016) 9759–9773.

[31] O. Rahman, S.C. Mohapatra, S. Ahmad, Fe_3O_4 inverse spinal super paramagnetic nanoparticles, Mater. Chem. Phys. 132 (2012) 196–202.

[32] Y. Wang, L. Wang, T. Tian, X. Hu, C. Yang, Q. Xu, Automated solid-phase extraction hyphenated to voltammetry for the determination of quercetin using magnetic nanoparticles and sequential injection lab-on-valve approach, Analyst 137 (2012) 2400–2405.

[33] M. Dehghan, A. Motaharinejad, M. Saadat, R. Ahdenov, M. Babazadeh, R. Hosseinzadeh-Khanmiri, Novel approach to synthesizing polymer-functionalized Fe_3O_4/SiO_2-NH_2 via an ultrasound-assisted method for catalytic selective oxidation of alcohols to aldehydes and ketones in a DMSO/water mixture, RSC Adv. 5 (2015) 92335–92343.

[34] S. Yang, T. Zeng, Y. Li, J. Liu, Q. Chen, J. Zhou, Y. Ye, B. Tang, Preparation of graphene oxide decorated Fe_3O_4@SiO_2 nanocomposites with superior adsorption capacity and SERS detection for organic dyes, J. Nanomater. 2015 (2015), http://dx.doi.org/10.1155/2015/817924 (Article ID 817924, 8 pages).

[35] F. Liu, F. Niu, N. Peng, Y. Su, Y. Yang, Synthesis characterization, and application of Fe_3O_4@SiO_2–NH_2 nanoparticles, RSC Adv. 5 (2015) 18128–18136.

[36] S.A. Kulkarni, P.S. Sawadh, P.K. Palei Synthesis, Characterization of superparamagnetic Fe_3O_4@SiO_2 nanoparticles, J. Korean Chem. Soc. 58 (2014) 100–104.

[37] F. He, J. Fan, D. Ma, L. Zhang, C. Leung, H.L. Chan, The attachment of Fe_3O_4 nanoparticles to graphene oxide by covalent bonding, Carbon 48 (2010) 3139–3144.

[38] S. Verma, H.P. Mungse, N. Kumar, S. Choudhary, S.L. Jain, B. Sain, O.P. Khatri, Graphene oxide: an efficient and reusable carbocatalyst for aza-Michael addition of amines to activated alkenes, Chem. Commun. 47 (2011) 12673–12675.

[39] W.-C. Oh, F.-J. Zhang, Preparation and characterization of graphene oxide reduced from a mild chemical method, Asian J. Chem. 23 (2011) 875–879.

[40] S. Narksitipan, S. Thongtem Synthesis, Characterization of transparent graphene oxide nanosheets, Ferroelectr., Lett. Sect. 41 (2014) 94–99.

[41] Y. Li, X.-Y. Wang, X.-P. Jiang, J.-J. Ye, Y.-W. Zhang, X.-Y. Zhang, Fabrication of graphene oxide decorated with Fe_3O_4@SiO_2 for immobilization of cellulase, J. Nanopart. Res. 17 (2015), http://dx.doi.org/10.1007/s11051-014-2826-z.

[42] J.A. Lopez, F. González, F.A. Bonilla, G. Zambrano, M.E. Gómez, Synthesis and characterization of fe 3 o 4 magnetic nanofluid, Rev. Latin Am. Metal. Mater. 30 (2010) 60–66.

[43] M. Wojtoniszak, X. Chen, R.J. Kalenczuk, A. Wajda, J. Lapczuk, M. Kurzewski, M. Drozdzik, P.K. Chu, E. Borowiak-Palen, Synthesis, dispersion, and cytocompatibility of graphene oxide and reduced graphene oxide, Colloids Surf., B 89 (2012) 79–85.

[44] R. Rahimi, A. Maleki, S. Maleki, Preparation of magnetic fluorochromate hybrid nanomaterials with triphenylphosphine surface modified iron oxide nanoparticles and their characterization, J. Magn. Magn. Mater. 355 (2014) 300–305.

[45] M. Hatamzadeh, M. Johari-Ahar, M. Jaymand, In situ chemical oxidative graft polymerization of aniline from Fe3O4 nanoparticles, Int. J. Nanosci. Nanotechnol. 8 (2012) 51–60.

[46] A. Alizadeh, M.M. Khodaei, M. Beygzadeh, D. Kordestani, M. Feyzi, Biguanide-functionalized Fe_3O_4/SiO_2 magnetic nanoparticles: an efficient heterogeneous organosuperbase catalyst for various organic transformations in aqueous media, Bull. Korean Chem. Soc. 33 (2012) 2546–2552.

[47] S.E. Moradi, Enhanced hydrogen adsorption by Fe_3O_4-graphene oxide materials, Appl. Phys. A 119 (2015) 179–184.

[48] P. Marques, G. Gonçalves, S. Cruz, N. Almeida, M. Singh, J. Grácio, A. Sousa, Functionalized graphene nanocomposites, in: A. Hashim (Ed.), Advances in Nanocomposite Technology, InTech, Rijeka, 2011(Ch. 11).

[49] J. Wang, S. Zheng, Y. Shao, J. Liu, Z. Xu, D. Zhu, Amino-functionalized Fe_3O_4@SiO_2 core-shell magnetic nanomaterial as a novel adsorbent for aqueous heavy metals removal, J. Colloid Interface Sci. 349 (2010) 293–299.

[50] S. Zhang, Y. Zhang, J. Liu, Q. Xu, H. Xiao, X. Wang, H. Xu, J. Zhou, Thiol modified Fe_3O_4@SiO_2 as a robust high effective, and recycling magnetic sorbent for mercury removal, Chem. Eng. J. 226 (2013) 30–38.

[51] M. Kruk, M. Jaroniec, Gas adsorption characterization of ordered organic-inorganic nanocomposite materials, Chem. Mater. 13 (2001) 3169–3183.

[52] K.S. Sing, Reporting physisorption data for gas/solid systems with special reference to the determination of surface area and porosity (Recommendations 1984), Pure Appl. Chem. 57 (1985) 603–619.

[53] Y. Li, Q. Du, T. Liu, X. Peng, J. Wang, J. Sun, Y. Wang, S. Wu, Z. Wang, Y. Xia, L. Xia, Comparative study of methylene blue dye adsorption onto activated carbon graphene oxide, and carbon nanotubes, Chem. Eng. Res. Des. 91 (2013) 361–368.

[54] J. Ma, M. Yang, F. Yu, J. Zheng, Water-enhanced removal of ciprofloxacin from water by porous graphene hydrogel, Sci. Rep. 5 (2015), http://dx.doi.org/10.1038/srep13578 (Article number: 13578).

[55] S. Stankovich, D.A. Dikin, R.D. Piner, K.A. Kohlhaas, A. Kleinhammes, Y. Jia, Y. Wu, S.T. Nguyen, R.S. Ruoff, Synthesis of graphene-based nanosheets via chemical reduction of exfoliated graphite oxide, Carbon 45 (2007) 1558–1565.

[56] E.T. Mombeshora, R. Simoyi, V.O. Nyamori, P.G. Ndungu, Multiwalled carbon nanotube-titania nanocomposites: understanding nano-structural parameters and functionality in dye-sensitized solar cells, S. Afr. J. Chem. 68 (2015) 153–164.

[57] Z.A. ALOthman, A review: fundamental aspects of silicate mesoporous materials, Materials 5 (2012) 2874–2902.

[58] L. Yang, P. Zou, J. Cao, Y. Sun, D. Han, S. Yang, G. Chen, X. Kong, J. Yang, Facile synthesis and paramagnetic properties of Fe_3O_4@SiO_2 core-shell nanoparticles, Superlattices Microstruct. 76 (2014) 205–212.

[59] N. Kumar, H. Mittal, V. Parashar, S.S. Ray, J.C. Ngila, Efficient removal of rhodamine 6G dye from aqueous solution using nickel sulphide incorporated polyacrylamide grafted gum karaya bionanocomposite hydrogel, RSC Adv. 6 (2016) 21929–21939.

[60] I.A. Lawal, B. Moodley, Column, kinetic and isotherm studies of PAH (phenanthrene) and dye (acid red) on kaolin modified with 1-hexyl, 3-decahexyl imidazolium ionic liquid, J. Environ. Chem. Eng. 4 (2016) 2774–2784.

[61] H.N. Tran, S.-J. You, A. Hosseini-Bandegharaei, H.-P. Chao, Mistakes and inconsistencies regarding adsorption of contaminants from aqueous solutions: a critical review, Water Res. 120 (2017) 88–116.

[62] X. Chen, Modeling of experimental adsorption isotherm data, Information 6 (2015) 14–22.

[63] Y.S. Ho, J.F. Porter, G. McKay, Equilibrium isotherm studies for the sorption of divalent metal ions onto peat: copper, nickel and lead single component systems, Water Air Soil Pollut. 141 (2002) 1–33.

[64] E.J. Billo, Nonlinear Regression Using the Solver. in Excel for Chemists®, John Wiley & Sons Inc., 2011, pp. 463–488.

[65] S. Álvarez, R.S. Ribeiro, H.T. Gomes, J.L. Sotelo, J. García, Synthesis of carbon xerogels and their application in adsorption studies of caffeine and diclofenac as emerging contaminants, Chem. Eng. Res. Des. 95 (2015) 229–238.

[66] M.H. Dehghani, M. Mohammadi, M.A. Mohammadi, A.H. Mahvi, K. Yetilmezsoy, A. Bhatnagar, B. Heibati, G. McKay. Equilibrium, Kinetic studies of trihalomethanes adsorption onto multi-walled carbon nanotubes, Water, Air, Soil Pollut. 227 (2016) 332.

[67] J. Fan, X. Ran, Y. Ren, C. Wang, J. Yang, W. Teng, L. Zou, Y. Sun, B. Lu, Y. Deng, D. Zhao, Ordered mesoporous carbonaceous materials with tunable surface property for enrichment of hexachlorobenzene, Langmuir 32 (2016) 9922–9929.

[68] M.-H. To, P. Hadi, C.-W. Hui, C.S.K. Lin, G. McKay, Mechanistic study of atenolol: acebutolol and carbamazepine adsorption on waste biomass derived activated carbon, J. Mol. Liq. 241 (2017) 386–398.

[69] V.K. Gupta, I. Ali, Removal of endosulfan and methoxychlor from water on carbon slurry, Environ. Sci. Technol. 42 (2008) 766–770.

[70] B.I. Kharisov, H.V. Rasika Dias, O.V. Kharissova, V. Manuel Jimenez-Perez, B. Olvera Perez, B. Munoz Flores, Iron-containing nanomaterials: synthesis properties, and environmental applications, RSC Adv. 2 (2012) 9325–9358.

[71] S. Álvarez-Torrellas, R.S. Ribeiro, H.T. Gomes, G. Ovejero, J. García, Removal of antibiotic compounds by adsorption using glycerol-based carbon materials, Chem. Eng. J. 296 (2016) 277–288.

[72] O.O. Nalcaci, N. Böke, B. Ovez, Comparative study on the removal of various phenoxyalkanoic acid herbicides from aqueous solutions on polycaprolactone and activated carbon, J. Environ. Eng. 137 (2011) 1136–1144.

[73] M. Essandoh, D. Wolgemuth, C.U. Pittman, D. Mohan, T. Mlsna, Adsorption of metribuzin from aqueous solution using magnetic and nonmagnetic sustainable low-cost biochar adsorbents, Environ. Sci. Pollut. Res. 24 (2017) 4577–4590.

[74] Débora de Almeida Azevedo, Sílvia Lacorte, Tereza Vinhas, Paula Viana, Damiá Barceló, Monitoring of priority pesticides and other organic pollutants in river water from portugal by gas chromatography–mass spectrometry and liquid chromatography–atmospheric pressure chemical ionization mass spectrometry, J. Chromatogr. A 879 (1) (2000) 13–26, http://dx.doi.org/10.1016/S0021-9673(00)00372-1.